2018

# Acoustic Emission Detection In 304H Stainless Steel Due To Intergranular Stress Corrosion Cracking

Joseph W. Hill
*University of South Carolina*

# ACOUSTIC EMISSION DETECTION IN 304H STAINLESS STEEL DUE TO INTERGRANULAR STRESS CORROSION CRACKING

by

Joseph W. Hill

Bachelor of Science
Florida Gulf Coast University, 2006

Bachelor of Science
Florida Gulf Coast University, 2016

---

Submitted in Partial Fulfillment of the Requirements

For the Degree of Master of Science in

Civil Engineering

College of Engineering and Computing

University of South Carolina

2018

Accepted by:

Paul Ziehl, Director of Thesis

Sarah Gassman, Reader

Juan Caicedo, Reader

Cheryl L. Addy, Vice Provost and Dean of the Graduate School

# DEDICATION

I dedicate this work to my wife Krystal, my parents Thomas and Gail, and my sister Elizabeth. I would not have been able to accomplish my goals of higher learning or pursuing a path to a successful and fulfilling career without their patience and support through these lean years.

# ACKNOWLEDGMENTS

I would like to thank my committee chair, Dr. Paul Ziehl, and committee members, Dr. Sarah Gassman, and Dr. Juan Caicedo, for their guidance and support through the process of my research and course work.

In addition, I would also like to thank my friends, colleagues, the department faculty and staff for making my time at the University of South Carolina a wonderful experience. Specifically, I would like to thank my colleagues PhD. candidate Rafal Anay, PhD. candidate Vafa Soltangharaei, and PhD. student Li Ai for their support over the past two years. Without the help of Dr. Ziehl and these three gentlemen, I would not have gained the knowledge and experience with this subject matter in the required time frame.

I would like to express my gratitude to the Bruce Greer, Senior Technical Leader at NDE Innovation, Electrical Power Research Institute, for his assistance and guidance with specimens, testing, and giving me exposure to other nondestructive testing methods used in the field.

Finally, I would like to acknowledge the University of South Carolina Graduate School, the Department of Civil and Environmental Engineering, the Electrical Power Research Institute, the Naval Engineering Education Consortium and the R.L. Sumwalt, Senior Endowed Fund for their financial support.

# ABSTRACT

Storage of spent nuclear fuel has become problematic in past decades due to delayed completion of long-term repositories for various reasons. Temporary storage containers called Dry Cask Storage Systems (DCSS) made of stainless-steel and surrounded by reinforced concrete have been in use but are exceeding their designed usage periods. Defects in canisters can be exacerbated in climates susceptible to high humidity and salinity levels. As inspection and relicensing of DCSS increases, more efficient monitoring techniques could save nuclear facilities valuable time and resources. Crack detection of the canister walls or welds in real time may be possible utilizing acoustic emission (AE) sensors. The capability to detect a partial-wall crack with an ASME-accepted, nondestructive testing method could prove useful for future DCSS inspection purposes.

The focus of this work, which is a part of a larger study for determining the feasibility of AE monitoring for DCSS, utilizes a small-scale type 304H stainless-steel specimen to monitor stress corrosion cracking. The plate specimen was statically loaded, creating a bending behavior which produced tensile stress at one face. A corrosive solution of potassium tetrathionate was then introduced to an electrical discharge machined starter notch and monitored for AE activity until crack initiation and propagation commenced. The raw wideband AE data was filtered and processed manually using proprietary software. Resonant AE data was filtered by hit count, duration and signal strength. Source

location of the emissions was performed by triangulation of event arrivals at the AE sensors. Cracking was also observed via digital microscopic evidence throughout the testing period.

The waveform patterns observed after testing resembled AE related to crack initiation and propagation in various materials, where the amplitude of the waveform increases suddenly near the beginning of the signal and then dissipates with time as the wave travels through the medium.

The frequency spectrum of these waveforms was determined using the Fast Fourier Transform. The peak magnitude of the observed signal frequencies fell within range of 100-300 kHz for the small-scale specimens. The mean frequency was 224 kHz with a standard deviation of 52.1 kHz.

Future work should include investigation of a larger-scale specimen more representative of an actual DCSS canister, while using a similar procedure. This will more accurately replicate field conditions and determine the possibility of detecting an emission traveling the length of a canister (approximately 16 feet). Furthermore, this test would help determine the feasibility of real-time AE monitoring.

TABLE OF CONTENTS

# LIST OF TABLES

# LIST OF FIGURES

# CHAPTER 1. INTRODUCTION

Power generation is a global necessity delivered to populations through various means. Renewable energy technologies are at the forefront of innovation and new investment, but nuclear power generation still accounts for nearly 20% of all power production in the United States according to the U.S. Energy Information Administration (USEIA 2017). Most of the US nuclear power plants currently in use were constructed in the 1960s, 1970s, and 1980s. This puts the average age of nuclear facilities in the United States at approximately 36 years. Nuclear power plants have massively complex systems and after running for many decades are bound to experience operational fatigue issues. Maintaining acceptable equipment conditions is especially crucial in these facilities for limiting radiation exposure to workers and the environment during production. Likewise, great care is taken to house the spent fuel byproducts (USC 2013).

The long-term plan for spent nuclear fuel is storage in geological repositories, such as the Yucca Mountain nuclear waste repository before closure in April 2011 due to negative public perception and political red-tape (SLER 2013). Until these facilities are built and licensed, however, the spent fuel must be stored in cooling pools and dry cask storage systems, abbreviated "DCSS" (USNRC 2017). DCSS started being used in the 1970s and early 1980s as an alternative storage option while the spent-fuel pools began filling to capacity. The spent fuels are placed within stainless-steel canisters, then water and air are removed and replaced by inert gas. Figure 1.1 shows an illustration of a dry

cask system. The stainless-steel canisters are sealed, typically by welding or bolting one end shut to provide a leak-proof environment, and then encased in a protective reinforced concrete cladding (UCS 2013). A gap remains between the steel and concrete layers to allow air flow for cooling. The goal of the cask system is to prevent any radiation from escaping and provide safe storage. Many DCSS licenses that originally allotted 20-years of use have reach their expiration (USNRC 2017). These casks are being inspected and relicensed for another 40-years in some cases. Current expectations are such that every U.S. nuclear facility will require the use of licensed DCSS by 2025, and according to the United States Nuclear Regulatory Commission, there are currently more than 2,500 casks in operation in the United States (USNRC 2017).

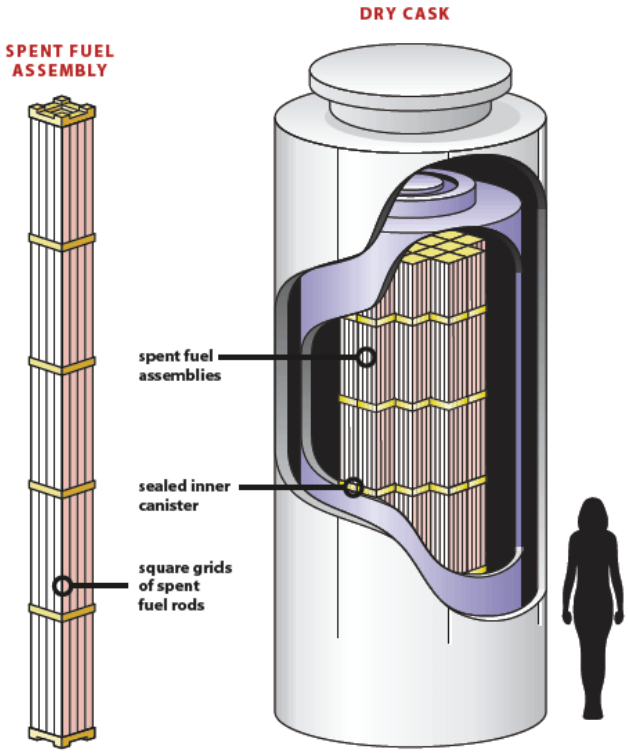


*Figure 1.1: Typical dry cask storage system assembly (UCS 2013, reproduced with permission)*

DCSS require inspections as part of the licensing process for continued use to ensure cask durability and longevity (USNRC 2017). This is particularly important for those located in unfavorable climates or near severe weather events (earthquake, flood, wind projectiles, and extreme temperatures). Additionally, casks used for extended periods in coastal regions may be more susceptible to corrosion of the metals. Material selection for the casks is paramount and the 300-series austenitic stainless-steel has proven to be a valuable metal for these applications due to its favorable mechanical properties and exceptional corrosion resistance.

Over time stainless-steel will become susceptible to certain types of corrosion, such as stress corrosion cracking, crevice corrosion, intergranular attack and weld decay (BSAA n.d.). Many of these corrosion conditions are triggered by stresses on the material in chloride rich environments (BSAA n.d.). Stress corrosion cracking will occur on surfaces in tensile stressed situations and in welded sections (BSAA n.d.). Crevice corrosion, also in chloride rich situations, tends to occur in tight spaces (between a surface and bolt head or washer) with less oxygen availability and depends on geometry (BSAA n.d.). Intergranular corrosion and weld decay occur when austenitic materials are exposed to heat (450-850°C) for prolonged periods of time (BSAA n.d.). The steel becomes "sensitized" when the carbon diffuses to the grain boundary, precipitating chromium carbide which affectively removes the chromium from the boundary (BSSA n.d.). Thus, the steel is now sensitized to corrosive environments. This phenomenon is also known as weld decay.

With the indefinite use of DCSS, identification of deficiencies is very important. More efficient and effective methods of damage detection need to be developed for inspection purposes. Additionally, some casks are stored underground, and all are partially

encased in concrete, making inspection of the stainless-steel canister more challenging. The idea of this study is to investigate and develop capabilities to detect a partial-wall crack with an ASME-accepted nondestructive testing method.

Nondestructive testing (NDT) refers to methods for evaluation of structural materials for defects while not altering their ability to operate and/or without imposing damage to them. NDT is ideal for ensuring the safety and integrity of structures that are in use and cannot feasibly afford interruptions. NDT is also used in manufacturing industries for quality control purposes.

Acoustic emission is one nondestructive testing method that has shown promising results over the past decades and researchers are devoting time and resources into this field of study. The mechanism of acoustic emission can be summed up as follows:

> *The origin of the acoustic emission technique lies in the phenomenon of rapid release of energy within a material in the form of a transient elastic wave resulting from dynamic changes like deformation, crack initiation and propagation, leakage etc. (Raj et al. 2000).*

Furthermore, ASTM International has recognized AE as a nondestructive testing method and defined it as transient elastic waves within a material caused by the release of localized stress energy (ASTM E 1316).

Figure 1.2 shows an elementary schematic of AE phenomenon whereby a fault or crack in the material creates a stress wave which propagates away from the crack as a load is being applied. As the wave travels outward and passes a sensor, it creates a disturbance or displacement in the sensor, converting it into an electric signal. The signal can be collected for further evaluation and analysis.

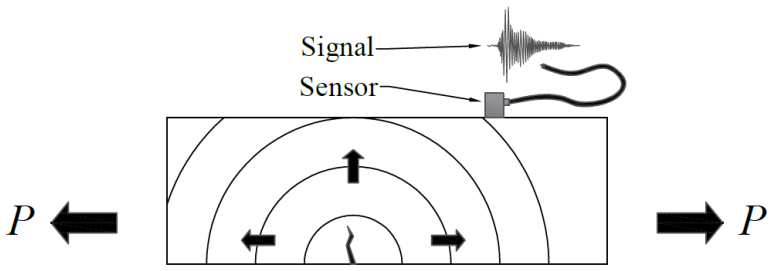


*Figure 1.2: Schematic of acoustic emission parameters*

Acoustic emission techniques have an advantage over other NDT methods, whereby they can evaluate specimens of large volume with relatively minimal instrumentation. In some cases, like the casks mentioned above, a single AE sensor could potentially be placed on the container to monitor for defects as they occur in real-time.

Structural applications for acoustic emissions are often related to cracking in a material. Therefore, experimentally generating AE events typically involves applying stresses to a material via loading (or unloading). Herein lies a potential disadvantage of acoustic emissions. Its dependency on loading means that a crack may not be detected. For example, a bridge that has a significant crack capable of producing AE waves during loading, would likely not produce detectable emission data unless it is stressed in some manner. These stresses would produce emissions in the form of movement at the crack.

In this study, acoustic emission signal recognition and frequency characterization was explored by way of crack initiation and propagation in type 304 stainless-steel. Stress corrosion cracking was induced by eccentric loading, creating tensile stresses on the face of a 304H austenitic stainless-steel plate, and exposing it to a corrosive potassium tetrathionate solution.

# CHAPTER 2. LITERATURE REVIEW

Dry cask storage systems for nuclear waste are being used more than ever due to the delay of permanent repositories (USNRC 2017). Since they require periodic relicensing, it is paramount to detect any defects that may develop over the decades of use. Research is being conducted to develop innovative and more efficient methods to carry out these tasks. This study will focus on developing a capability to detect a partial-wall crack with an ASME-accepted, nondestructive testing method.

Nondestructive testing (NDT) methods are important for evaluating the integrity of structures or materials without inflicting any damage. Due to the sensitive contents of the casks, a NDT method is required to detect defects in the steel canisters, such as cracking through the wall thickness or within the welds. These defects are sometimes caused by way of corrosion over time because of the environments in which they may be stored.

Since the utilization and relicensing of these casks has continued, a variety of studies have taken place over recent decades. The following discussion covers some of these and how their methods can be used for similar work in this thesis.

## 2.1 ACOUSTIC EMISSION NOISE AND CRACK TYPE DIFFERENTIATION

AE has an unavoidable characteristic that adds to the difficulty of detecting events related to faults in materials. This is often referred to as noise, or any AE event that is not

related to the desired signals derived from defect or cracking signals. Depending on the application, typical noise emissions from normal operations or background occurrences are significantly lower in peak amplitude than those from cracks or faults in a material (Hossain et al. 2013). Noise emissions come from many different sources and they typically occur in much greater quantities than emissions from faults. Examples of noise include friction from moving mechanical parts, vehicles traversing a bridge, and fluids passing by the material. The noise emissions require filtering since most are not relevant for the detection of faults. Amplitude is the governing parameter of determining whether a wave is from a fault or noise. Through observation of noise amplitudes, a threshold can be created to filter some of them from the data (Hossain et al. 2013).

Acoustic emission testing has been a hot topic as an alternative non-destructive testing method due to its potential applications for aging, in-service structures. Though AE has shown success in different types of materials, this literature review will focus on metals.

Aggelis et al. (2011) conducted an experiment using broadband sensors, meaning they have the capability of recording a broad range of frequencies. This was performed on aluminum plate coupons during tensile testing. They analyzed the RA value (a ratio of rise time to waveform amplitude) and observed a variation in the AE signal behavior as the sample transitioned from tensile failure into shear failure (Aggelis et al. 2011). This was confirmed by the failure mode in the sample which displayed a common fracture pattern in thin notched metal coupons (Aggelis et al. 2011). The observed information was used to propose a tool for predicting an ultimate life for materials under fatigue. This study reinforced the idea that AE signals from varying types of fatigue cracking growth emit

different signatures that can be identified and assigned accordingly (Aggelis et al. 2011).

Amer et al. (2013) investigated the damage mechanisms that control the useful lifetime of 304L stainless-steels typically used in nuclear componentry. They did so by attempting to differentiate AE signatures related to plastic deformation and fatigue cracking when subject to cyclic loading. Low-cycle fatigue tests were conducted on the material using a servo-hydraulic machine (MTS 810) at different strain levels. They considered two methods of analysis, the conventional analysis of the amplitude of strain imposed on the specimen, and a multivariate statistical analysis where the signals are segmented into groups using the technique of k-means. The difference between fatigue crack growth and plastic deformation in the steel could be distinguished by observing the total strain amplitude in the signal (Amer et al. 2013). They found agreement with previous work where AE signals could be identified and categorized by their unique signatures. The AE data was broken down into three categories (or clusters). Cluster 1 had low and constant cumulative energy which they related to plastic deformation at the head of a crack tip (Amer et al. 2013). Cluster 2 increased at a slow rate and then increased exponentially toward the end of testing, consistent with crack propagation during fatigue (Amer et al. 2013). The third set of emissions, Cluster 3, occurred only toward the end of the test and showed low cumulative energy, and the authors linked this behavior to martensitic phase transformation (Amer et al. 2013).

Fatigue cracking control is very important regarding steel used in nuclear applications such as blanket applications in fusion reactors. Specialized metals for use in these applications include reduced activation ferritic-martensitic steel (Babu et al. 2016). Reinforcing other findings, Babu et al. (2016) performed AE testing on this metal and

found similar discontinuities in signals related to cracking and crack closure (Babu et al. 2016). The authors observed intergranular cracking in the metal with higher quantities of hits and peak amplitude at ranges of 66-88 dB and also observed differences in cracking and closure, where fatigue crack growth hits showed two groups of signals at higher values of stress intensity factor range (Babu et al. 2016). On the other hand, crack closure and transition showed one signal group with lower stress intensity (Babu et al. 2016).

## 2.2 STRESS CORROSION CRACKING

In a 2007 study by Shaikh, et al., stress corrosion cracking (SCC) in 316LN stainless-steel was evaluated using AE for specimens in compact tension tests in accordance with ASTM E399. The goal was to determine micro-process mechanism which initiates the SCC. The stainless-steel was subject to loading stress in a 45% $MgCl_2$ solution (weak acid) at a temperature of 413K. Their results included a steel crack growth rate of 2.33x10-8 m/s with AE amplitude ranging from 27.6 to 46.5 dB (Shaikh et al. 2007). The emissions were continuous prior to crack initiation, identified by increased energy and counts, while the time gap between events increased during initiation (Shaikh et al. 2007). In other words, as the crack propagation grew, so did the spaces in time between AE events. They concluded that most of the AE activity was due to plastic deformation at the tip ahead of the crack and found that cracking propagated in a trans-granular fashion (Shaikh et al. 2007).

Another study by Du et al. (2011) looked at the process of corrosion in 304 stainless-steel using slightly acidic sodium chloride (NaCl) solution during slow strain rate testing. The authors monitored the specimen during testing using electrochemical noise and acoustic emission techniques. They could produce gradual stress corrosion cracks at

localized areas in the specimens and monitored them using both methods (Du et al. 2011). They concluded that using either method produced a similar result and proposed using both for on-site reliability in real world applications (Du et al. 2011). The acoustic emission signals were characterized according to different sources (pitting, cracking, and bubbling) and could aid in analyzing different effects of corrosion (Du et al. 2011). The authors found that the solution used (1.5 mol/L $H_2SO_4$ + 0.5 mol/L NaCl) to produce the corrosion defects in the 304NG stainless-steel could reliably cause SCC in the specimens (Du et al. 2011).

Further evidence in salt solution successfully producing SCC cracking in stainless-steel was found in a study by Gomez-Duran and MacDonald (2006), where the noise of the coupling current was studied in sensitized type 304 stainless-steel exposed to a thiosulphate solution (0.5 M). Once testing concluded, the authors found that sodium thiosulphate solution (0.5 mol/L $Na_2S_2O_3 \cdot 5H_2O$) was capable of SCC propagation under loaded and unloaded conditions. Loading simply increased the rate which the SCC occurred in the specimen (Gomez-Duran and MacDonald 2006).

Another study using type 304L stainless-steel was performed by Ghosh and Kain (2010) where they looked at the increased susceptibility of SCC on the surface of the machined steels when exposed to a chloride environment. They exposed a surface of the steel, after machining to a depth of 0.5mm, to solution (5.0 mol/L $H_2SO_4$ + 0.5 mol/L NaCl) at room temp until cracking occurred. The authors also exposed strips of the machined stainless-steel to boiling $MgCl_2$ solution in accordance with ASTM G36 to understand the residual stresses and strains resulting from surface machining and its propensity for SCC. They concluded that lathe machining (facing) of the metal refines the grain, which induces

plastic deformation and martensite transformation near the surface resulting in extremely fine grain size and work-hardening of the steel (Ghosh and Kain 2010). The study found that machining increases the rate of SCC when exposed to the solution (from 170 hours for non-machined, to 48 hours for the machined) (Ghosh and Kain 2010). Furthermore, they found that non-sensitized stainless-steel subject to high temperature and high aqueous environments, similar to conditions in boiling water reactors, developed intergranular SCC (Ghosh and Kain 2010).

A study in 2008 was conducted by Alverez et al. that looked at the AE signals produced in type AISI 304 stainless-steel in salt solution (1.0 mol/L NaCl + 1.0 mol/L HCl). The authors were interested in looking at differences in signals produced due to transgranular versus intergranular SCC in the type 304 steel, work that has been performed previously on brass by Lapitz et al (2007). They found that, like the brass, the transgranular crack propagation occurs with higher signal activity than the intergranular, and with the stainless-steel, they occurred on average with greater frequency on the order of one magnitude (Alverez et al. 2008). Likewise, they found that the two types of SCC have similar mean amplitude and rise time in the signals (Alverez et al. 2008). The authors believed that the increase in AE activity in SCC may be due to the mechanical tearing through the grain boundaries by the crack propagation (Alverez et al. 2008).

Marrow et al. (2006) performed a study to look at dynamics and morphology of intergranular SCC in sensitized austenitic stainless-steel (type 304). They simulated light water environments using two methods: a statically loaded specimen exposed to a stimulant potassium tetrathionate solution (0.15 mol/L $K_2S_4O_6$), and another in a high temperature and pressure autoclave. Tetrathionate stimulant solutions are used because they attack the

grain boundaries near the areas of greater chromium depletion (Marrow et al. 2006). They also modified the grain size and grain boundary character by way of cold-rolling (to introduce 30% strain) and thermo-mechanical (heat) treatment (Marrow et al. 2006). The heat treatment was performed by placing the specimen in an argon environment at approximately 900° C for thirty-minutes, followed by a water quench. This process adequately achieved the desired characteristic microstructure for their samples (Marrow et al. 2006).

An investigation into the effects of surface preparation methods and their susceptibility to result in SCC for type 304 stainless-steel was undertaken by Turnbull et al. (2011). Specimens were prepared using various methods including transverse grinding, longitudinal grinding, transverse dressing, and transverse milling. Simulation of nuclear power plants in a coastal region was achieved by exposing the samples to magnesium chloride solution ($MgCl_2$) and then placing them into a chamber with a relative humidity of 45% and temperature of 60° C. The stress in the specimens was created by way of four-point bending. Cracking occurred within pitted corrosion zones and pitting occurred in all types but was the greatest in the ground specimens (Turnbull et al. 2011).

## 2.3 AE FROM CRACKS IN WELDED JOINTS AND FATIGUE CRACKING

The use of acoustic emission methods for detecting faults has also proven valuable in welded joints of metals in addition to continuous members, particularly because cracking at welded sections can be difficult to diagnose with traditional methods. Welded sections have a higher occurrence of faults because of their discontinuities and "locked-in" stresses from the welding process and these factors can spur the initiation of fatigue cracking over

the useful life (Yu et al. 2013). Yu et al. (2013) designed a study to replicate a typical cruciform fillet welded joint found in steel bridges and analyzed acoustic emissions by varying the size of the base plate, and the stress ratio. The desired goal for varying these two factors was to determine their impact on the AE output from the structure. Noise reduction was handled by load pattern, source location, and wave-form feature analysis. While crack propagation was occurring, the AE signals observed from stable crack regions were slightly greater in intensity than those from the typical noise threshold (Yu et al. 2013). The signals from unstable crack regions, or what they termed "rough fracture surface", were detected with the highest intensity (Yu et al. 2013). Therefore, fatigue cracking was readily detected (Yu et al. 2013). The width of welds showed a difference in fatigue life (wider equated to longer life), but the AE signal intensity produced by the fatigue cracking was not affected by width (Yu et al. 2013). Finally, the authors recommend avoiding threshold-setting methods of AE hit quantification by way of absolute energy event observation (Yu et al. 2013).

Mazal et al. (2015) conducted an experimental study that focused on AE signals of fatigue cracking during cyclic loading in aluminum and titanium alloy metals, specifically on pre-initiation and then initiation of cracking. These results were compared to existing results of Inconel alloy (713LC) and steel used in nuclear reactors (15Ch2NMFA). They found that the AE signals translated to higher stresses during the pre-initiation stages and these stresses reduced once initiation and propagation of the fatigue cracking commenced (Mazal et al. 2015). By observing the AE amplitude and duration, they found that increased loading resulted in an increase in AE hits and growth of micro-cracks (Mazal et al. 2015). This led to their recognition of the promising potential for utilizing AE methods as an early

indicator for detecting fatigue cracking damage in metals (Mazal et al. 2015). They noted some of the dilemmas that are still evident in AE testing relating to the materials used, sensors used, coupling method, sensor location/arrangement, material geometry, etc. and these things need to be taken into consideration for experimental uniformity (Mazal et al. 2015).

## 2.4 OTHER AE RELATED LITERATURE: PREDICTING CRACK PROPAGATION FOR IN-SERVICE BRIDGES AND FAULT DETECTION IN MOVING MACHINERY

A correlation was found between AE absolute energy rate and crack growth rate which aided in better understanding and detecting crack growth behavior for in-service bridges (Yu et al. 2010). A better understanding in this area could greatly benefit the assessment of existing aging structures. Furthermore, specific algorithms were developed in this study to help eliminate the perceived false emissions along with noise reducing filters based on the Swansong II and a waveform-based approach. They found agreement between the actual cracking found in their ASTM A572G50 specimens and predicted modeling using the mentioned method which further verified their model and procedure (Yu et al. 2010). They concluded that the cumulative absolute energy and counts of AE (when combined with equations laid out in the literature) can effectively provide warning when fatigue cracking propagation is eminent (Yu et al. 2010). This could potentially help avoid catastrophic failure.

Yu and Ziehl (2012) utilized the previously mentioned absolute energy rate of AE along with other factors (stress intensity and fracture toughness) to predict crack growth behavior in stable and unstable crack stages for A572 structural steel. They used a load ratio to validate their presented model. Pattern recognition and analysis of waveform

features were used to distinguish crack growth signals from the noise. From a crack growth rate curve, a ratio was obtained and used to derive crack extension which could be used to estimate the remaining useful life. The authors concluded the presented models and procedures were effective at conservatively evaluating fatigue damage and can predict the remaining fatigue life in the specimen (Yu and Ziehl 2012). However, due to the complexities of in-service bridges, this method was not recommended for implementation in the field without further refinement (Yu and Ziehl 2012).

Acoustic emission testing has also gained recent momentum with its potential application in moving machinery. By utilizing AE signal discrimination, the desired application would be to develop acceptable methods for monitoring important and/or expensive equipment to catch faults or problems before catastrophic failure. This would potentially allow the owner to properly maintain it while avoiding the extra cost or downtime in the event of a major failure.

Danyuk et al. (2016) argue, that while AE testing done previously is an emerging method for potential non-destructive testing in moving or running machinery, signals with lower amplitudes are much harder to detect in industrial settings due to the high volume of noise present. They evaluated traditional threshold-based detection versus the "PhasePicker" algorithm, a threshold-less method of data acquisition and analysis to monitor fatigue crack initiation and propagation. Using the wavelet transform, this algorithm detected more signals than the more conventional threshold AE method (Danyuk 2016).

The application of acoustic emission has become attractive for use in rotational machinery as an alternative to vibration signals. Li and He (2012) developed a

methodology for this type of AE fault detection using empirical mode decomposition (EMD) based AE feature quantification. They conducted a case study using a gear box for fault detection for comparison to EMD results in previous studies and signals were extracted from the denoised signals and then fused into a single compressed AE feature. The work performed in the literature showed that the authors proposed method was more sensitive to fault recognition than the existing method (Li and He 2012).

Qu et al. (2014) conducted a comparative study of testing for gearbox faults using both AE based methods and more traditional vibration-based techniques using the same sampling rate for comparative purposes, even though AE typically utilizes higher sampling rates than vibration techniques (Qu et al. 2014). While both methods are viable means for achieving the detection of faults and both were effective in doing so, the AE could detect differences in the severity of gear tooth damage (Qu et al. 2014). Furthermore, AE signals showed stable performance and were insensitive to mechanical noise while vibration signals can be affected by mechanical resonance (Qu et al. 2014).

Another evaluation of AE and vibratory-based methods on gearboxes was conducted by Loutas et al. (2009). Like other studies, the AE method was found to be more effective than vibration recordings in some respects like early stage diagnosis of natural wear in gear systems (Loutas et al. 2009). A linear behavior of AE parameters was observed and was associated with changes in the crack propagation rate and the authors concluded that AE monitoring showed good potential for detecting early crack propagation for gearbox applications (Loutas et al. 2009).

# CHAPTER 3. PROCEDURE

## 3.1 ACTIVE TESTING, DATA ACQUISITION, AND PERIODIC MONITORING

Active testing and data acquisition took place in a small basement level room of the University of South Carolina. This room is isolated and secure for noise reduction, ideal for acoustic emission testing. The temperature and relative humidity are controlled for other testing taking place in the same space.

The testing procedure on the specimens spanned a period from March to May of 2018. The plates were tested consecutively which made the process run considerably smoother for the later specimen. Once all componentry was in place and the testing had commenced, the conclusion of active testing was dictated by visible cracking on the top (tensile stressed) surface of the plate. The first specimen was loaded and tested for AE activity for a duration of 16 days. The second specimen was tested for 19 days. Figure 3.1 shows the entire testing setup during active testing (except for the AE Acquisition software).

The test was monitored regularly for any abnormalities that may have affected the AE data recording and time-stamped when they transpired. Visual inspection of the plate surface also occurred on a regular basis (every 1-2 day) by pausing the system, removing the solution tube cover and any solution within the vessel, observing the bare surface by eye, photograph, and microscope, and then replacing the solution and resuming the acquisition process.

The following sections of chapter 3 describe in detail, the materials, instrumentation, and methods involved in carrying out small-scale specimen testing.

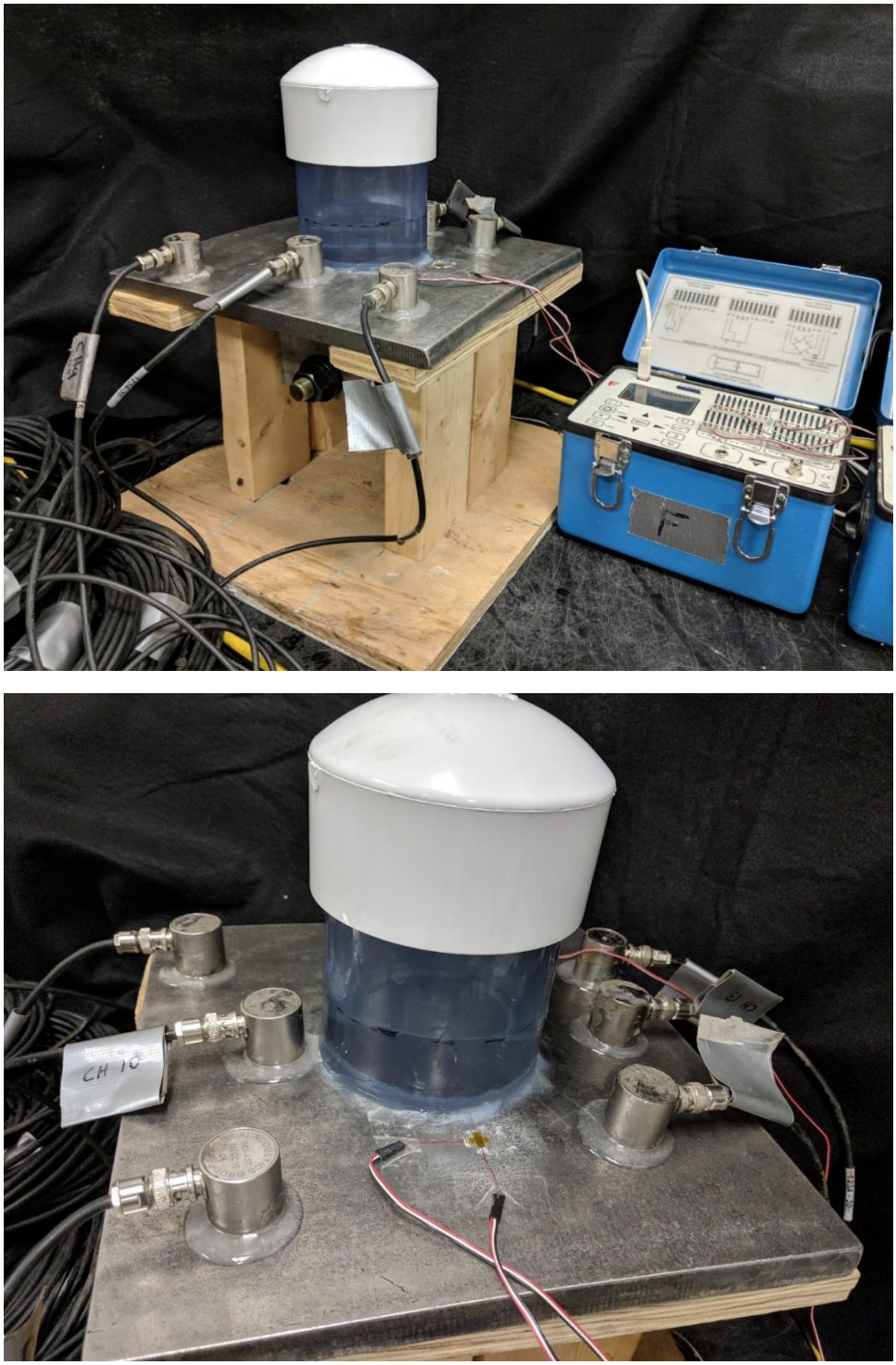


*Figure 3.1: Actual test setup*

## 3.2 TESTING SPECIMEN MATERIAL

The principle idea for this study was to gain further understanding for early detection of stress fractures and/or faults in stainless-steel materials that are typically used in dry cask storage systems (DCSS). This is of interest because many of the casks currently in use are experiencing lifespans which have past their originally projected operation period.

The testing discussed in this paper was a small-scale procedure. The latter phases should utilize larger sized stainless-steel materials, similar to those found in the actual DCSS. Many nuclear applications utilize type 304L stainless-steel (L for low carbon content, 0.035%). However, type 304H was used for testing because the properties of the two materials are nearly identical, but the higher carbon content of 304H would allow faster a corrosion process, thus a shorter testing period. The specimens used in this study were composed of 304H stainless-steel (H for high carbon), with a carbon content of 0.04-0.08% per volume. The dimensions of the specimens and the componentry used can be viewed in Figure 3.2 and the actual experimental setup is shown in Figure 3.3.

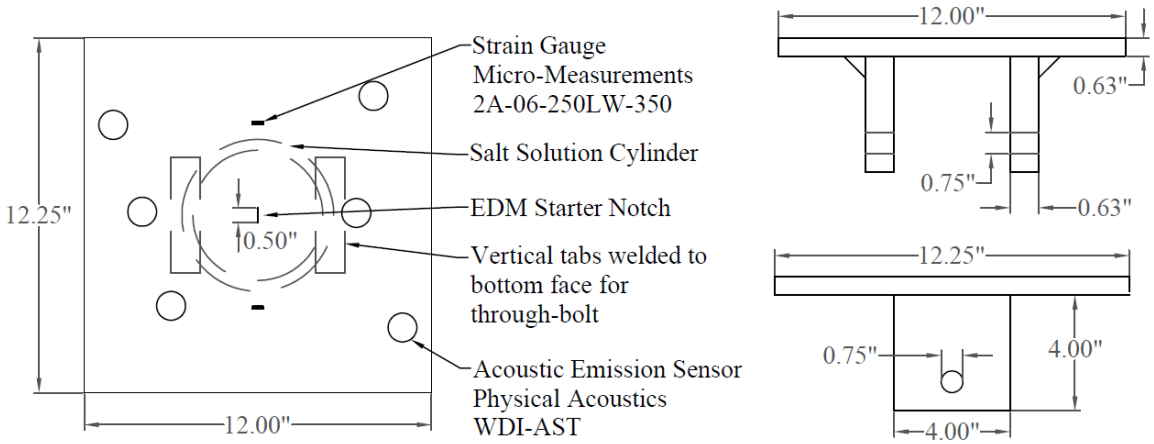


*Figure 3.2: Specimen dimensions and componentry*

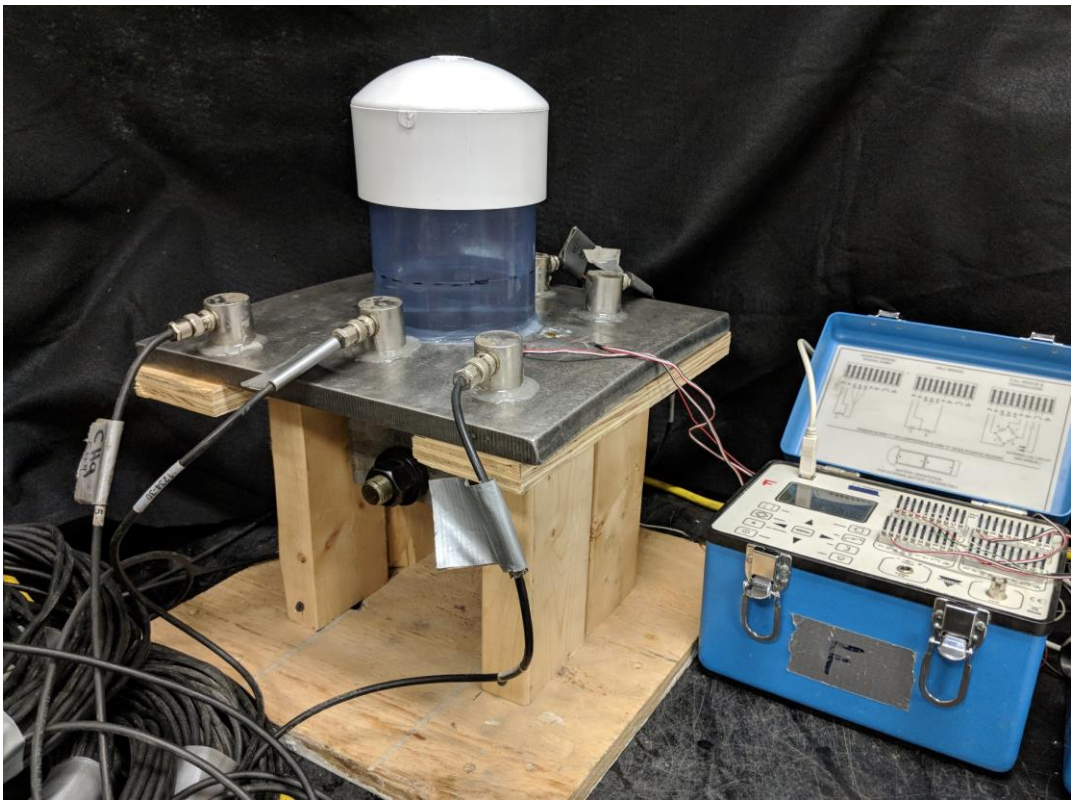

*Figure 3.3: Experimental setup*

The specimens are plates measuring 12 inches (305 mm) by 12.25 inches (311 mm) by 0.625 inch (16 mm) thick (Figure 3.4). They were fabricated with two perpendicular tabs on each specimen, 4 inches (102 mm) square, welded to the bottom face with a hole in each located 3 inches (76 mm) from the bottom-face of the plate. These holes allowed for 0.75 inches (19 mm) diameter bolt and nut to be inserted into the tabs. Once tightened, compressive forces squeeze the welded tabs toward one-another. This action creates bending within the plate, producing tension-faces and compression-faces on either side along the central axis between the welded tabs. This bending axis is where the desired cracking was produced via an electrical discharge machined (EDM) starter notch.

The desired outcome with this setup is to create sufficient stress in the top surface of the plates to create a partial crack through its thickness. While the tightened bolt experiences tensile stresses through its length, a compression stress is experienced in the welded tab portions of the specimen which transfers to the plate. Two stress factors must be considered for the stress calculation for the experiment. The first is purely compressive stress obtained by tightening the bolt. This is applied perpendicularly to the tabs and the cracking axis of the plate. Secondary stresses are produced by the moment created from the bolt positioning, which is 3 inches (76 mm) from the plate. These stresses transfer through the welds of the tabs, creating the bending mentioned above. The bending induces compressive stresses in the bottom fiber and tensile stresses in the top fiber at the location of the fabricated notch.

*Figure 3.4: 304H stainless-steel specimens with starter notch*

## 3.3 TARGET STRESS CALCULATION

When determining a proper stress for the specimens, it was important to ensure that yielding was avoided. Yielding would push the plate past its elastic threshold and into plastic behavior. Since 304H stainless-steel has a yielding stress around 30,000 psi (206 MPa) and the desire is to stress the plate without yielding, the target stress for this test was set at 27,000 psi (186 MPa). To accomplish the target stress in the plates, multiple measures were taken to ensure proper loading through the bolt.

The notch is aligned with the center axis of the plate in between the tabs. A tensile stress is required along this axis to produce the conditions suitable to induce cracking along this notch once a corrosive solution is applied. As the bolt at the bottom of the plate is tightened, it will apply axial stresses and bending stresses to the specimen. The stresses experienced at the extreme top and extreme bottom fibers of the plate can be calculated by:

$$\sigma_{target} = \sigma_{axial} + \sigma_{bending} \quad \text{(eq. 1)}$$

$$\sigma_{target} = -\frac{P}{A} + \frac{Mc}{I} \quad \text{(eq. 2)}$$

$$\sigma_{target} = -\frac{P}{A} + \frac{P*arm*c}{I} \quad \text{(eq. 3)}$$

$$\sigma_{target} = P\left(-\frac{1}{A} + \frac{arm*c}{I}\right) \quad \text{(eq. 4)}$$

where,

$\sigma_{target}$ = desired stress experienced in the plate
$P$ = load applied by bolt
$A$ = cross-sectional area of the plate
$M$ = the moment applied by the loading through the bolt; $M = P * arm$
$c$ = distance from neutral axis of the plate to the desired extreme fiber, and
$I$ = moment of inertia of the plate

Equation 4 can be rearranged to determine the loading applied to the plate which produced the target stress below the yielding of 304H stainless-steel. This target stress will occur for each face of the plate at different loads on the bolt due to its eccentricity from the neutral axis. The first face that experiences this stress will govern the loading, as to avoid any plastic behavior in the steel. Equation 5 and 6 determine the loading on the bolt which results in the target at the top face ($P_{tensile}$) and bottom face ($P_{compressive}$) of the plate, respectively.

$$P_{tensile} = \frac{\sigma_{target}}{-\frac{1}{A}+\frac{arm*c}{I}} \quad \text{(eq. 5)}$$

$$P_{compressive} = \frac{-\sigma_{target}}{-\frac{1}{A}-\frac{arm*c}{I}} \quad \text{(eq. 6)}$$

The compressive face proved to be the controlling factor. Using this information, the compressive loading can be substituted back into equation 3 to find the stress experienced at the top ($\sigma_{top}$) and bottom ($\sigma_{bottom}$) of the plate.

$$\sigma_{top} = -\frac{P_{compressive}}{A} + \frac{P_{compressive}*arm*c}{I} \quad \text{(eq. 7)}$$

$$\sigma_{bottom} = -\frac{P_{compressive}}{A} - \frac{P_{compressive}*arm*c}{I} \quad \text{(eq. 8)}$$

Strain gauges were utilized on the top face of the plate along the bending axis to verify that the bolt tightening corresponds to the calculated torque on the bolts. This strain at the top of the plate can be calculated using the material modulus of elasticity ($E$).

$$\varepsilon_{top} = \frac{\sigma_{top}}{E} \quad \text{(eq. 9)}$$

Separately, the torque ($T$) applied to the bolt to achieve the same stresses was calculated using equation 10.

$$T = k * D * F \quad \text{(eq. 10)}$$

where,

$k$ = bolt torque friction factor or nut factor (Lubricated bolt condition = 0.18)
$D$ = diameter of threaded bolt section, and
$F = P_{compressive}$ = applied force desired

The specific calculated results for this test and the material properties used can be reviewed in Appendix A.

## 3.4 POTASSIUM TETRATHIONATE SOLUTION

Applying a mechanical stress to the specimen is only part of the crack production process. A corrosive environment on the surface of the plate was also necessary for crack initiation. This involves using a mild acidic solution for controlled corrosion near the notched location.

Early testing involved a mild sodium thiosulfate ($Na_2S_2O_3$) salt solution exposed to the surface of the specimens. Nearly 60 days of contact produced no cracking in the plate. Therefore, a decision was made to switch to a slightly more corrosive solution. A Potassium tetrathionate ($K_2S_4O_6$) solution was used to induce cracking at the EDM notch. Two concentrations of the mixture were utilized, a 1% solution, or one-part potassium tetrathionate to ninety-nine-parts distilled water. The other was a 2% solution. Sulfuric acid was used to bring the solution pH levels to 3.0, necessary to create a reaction triggering the corrosion process.

A one-part (1%) solution was used for most of plate testing, while the 2-part (2%) solution was used only for a short period at the end of the testing in plate number 1. The visible corrosion of the exposed surface was more severe with higher concentration level. However, the solution concentration (1% versus 2%) did not appear to affect the rate of

cracking by any discernable amount.

## 3.5 SENSITIZATION OF STAINLESS STEEL

The objective is to induce and grow cracks in the specimen via corrosion within a reasonable time period. The subject material, 304H stainless-steel, is utilized in the manufacture of nuclear containment vessels due to its ability to prevent the phenomenon of corrosion. Thus, the specimens needed to be treated to allow for corrosion susceptibility. This can be achieved by way of sensitization heat treatment. Sensitization in stainless-steel is typically performed by increasing its temperature to a range of 400-850°C (750-1550°F). These specimens were heated to 675°C (1250°F) and held at temperature for a period of 14 hours in a vacuum furnace. By bringing some alloys (austenitic steels especially) up to their sensitization temperature, they are more vulnerable to intergranular corrosion. This occurs when some of the carbon in the material bonds with the chromium to form carbides. These carbides tend to form near the grain boundaries, and in turn, the grain boundaries become lacking in the protective chromium oxide layers in the stainless-steel material. The grain boundary is less resistive to corrosive activity since it is deficient in the corrosion resisting chromium. Changes in the sensitization process can be observed in Figures 3.5 and 3.6 for the specimens used in this testing (courtesy of Bruce Greer, Electrical Power Research Institute). The grain boundaries are visible in all figures. However, after 2 hours of sensitization, some of the boundaries are less visible where the carbide has yet to form. After the full 14 hours of sensitization has been applied to the stainless-steel, they are very pronounced because the chromium carbide has formed at more of the boundaries. One can notice the thick black outlines along the grain boundaries in the figures and how it differs

from the during-sensitization pictures (left), to the post-sensitization figures (right). It is possible for this process to occur in the cask manufacturing process when the materials are welded and experience large fluctuations in temperature.

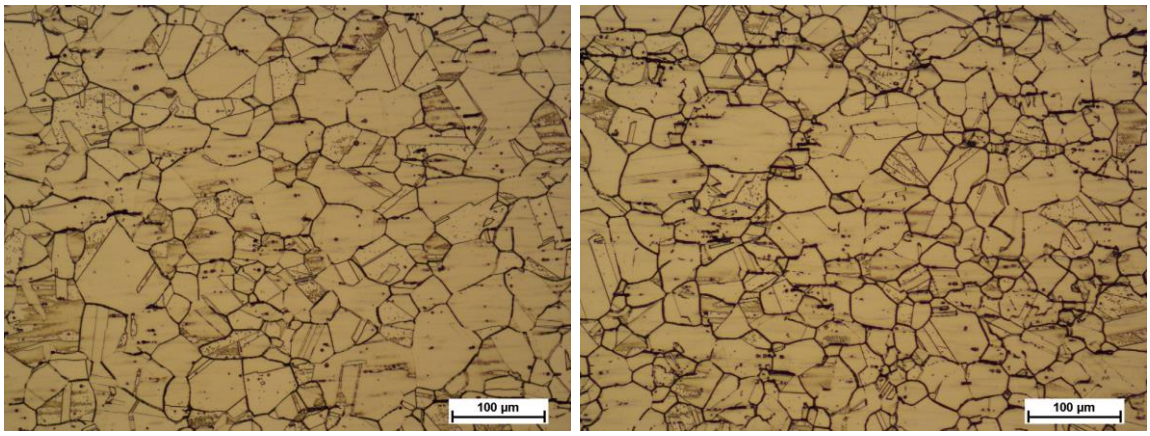


*Figure 3.5: Sensitization after 2 hours and 14 hours at 200-times magnification*

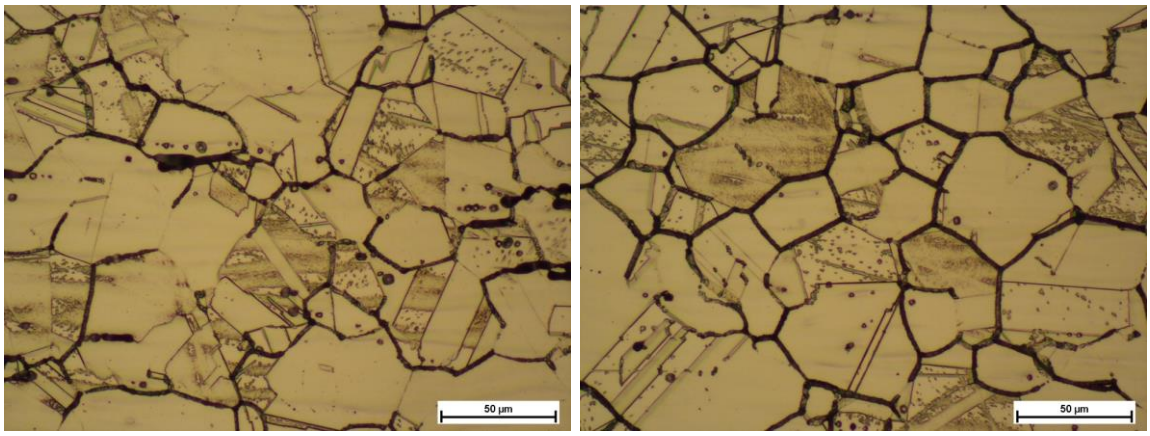


*Figure 3.6: Sensitization after 2 hours and 14 hours at 500-times magnification*

## 3.6 ELECTRICAL DISCHARGE MACHINED NOTCH

Electrical discharge machining (EDM), sometimes called spark machining, is a process where a section of subject material is removed by way of rapid high-frequency current discharges. Material is removed, or eroded, from the subject, in the shape of the electrode applied to the surface. This process is valuable for use in hard metals which are

less suitable for typical machining methods. The starter notches produced for crack propagation in these specimens measured 0.5 inch (12 mm) in length, 0.02 inch (0.5 mm) in width, and 0.04 inch (1 mm) in depth (Figure 3.7).

Once mechanical and environmental stresses are introduced, cracking initiated from the location of the notch due to the weaker discontinuity of the cross-section.

*Figure 3.7: Electrical discharge machined notch*

## 3.7 STRAIN MONITORING

Micro Measurement strain gauges (C2A-06250LW-350) were aligned perpendicular to the EDM starter notch axis for measurement of tensile strain in the top fiber of the stainless-steel specimens. The information collected from the gauges was recorded by a P3 Strain Indicator and Recorder (Figure 3.8), also manufactured by Micro Measurements (or Vishay Intertechnology, Inc.). This device is a portable, stand alone, recorder capable of acquiring data from four different gauges in real time, at varying sampling rates. The P3 system was used to acquire the strain gauges and bolt load cell data

once every 600 seconds (10 minutes). They were powered continuously without interruption.

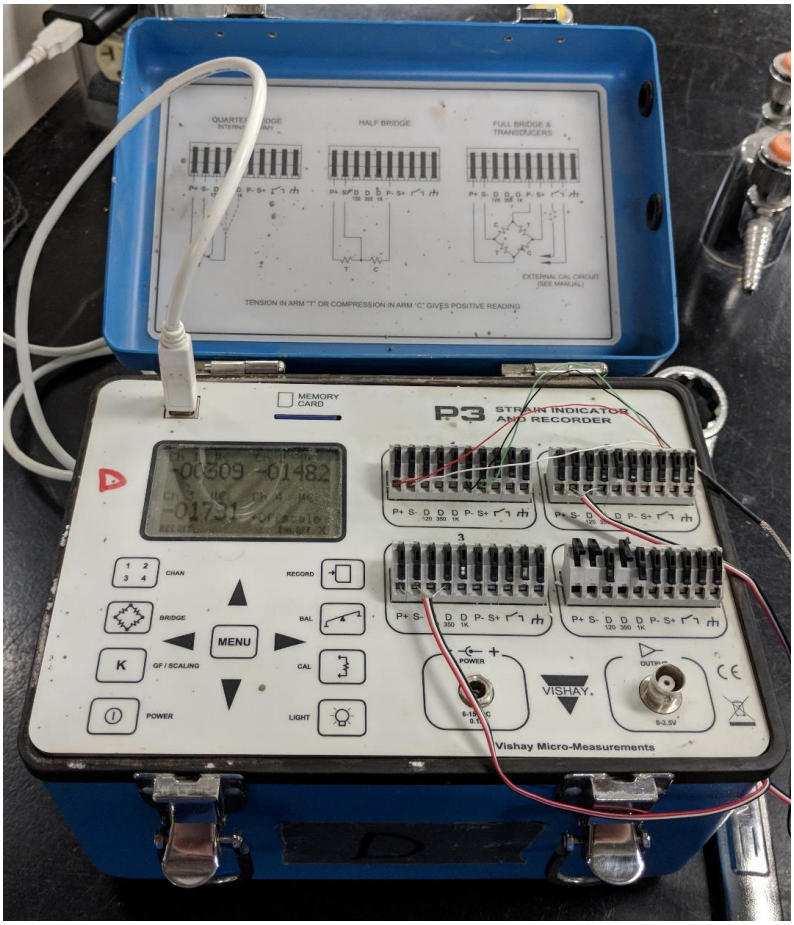


*Figure 3.8: Micro Measurements P3 strain indicator and recorder*

## 3.8 BOLT LOADCELL

A specialized ring-shaped load cell was used to monitor the axial loading onto the tabs attached to the bottom face of the plate (Figure 3.9). The loadcell is capable of fitting around the 0.75 inch diameter bolts. The cells were manufactured by Omega Engineering, Inc (model number LC901-3/4-65K) and have a maximum load capacity of 65 kips. Once

loaded, the cells respond by producing a voltage that can be monitored using a data acquisition system such as the P3 acquisition system used in this test.

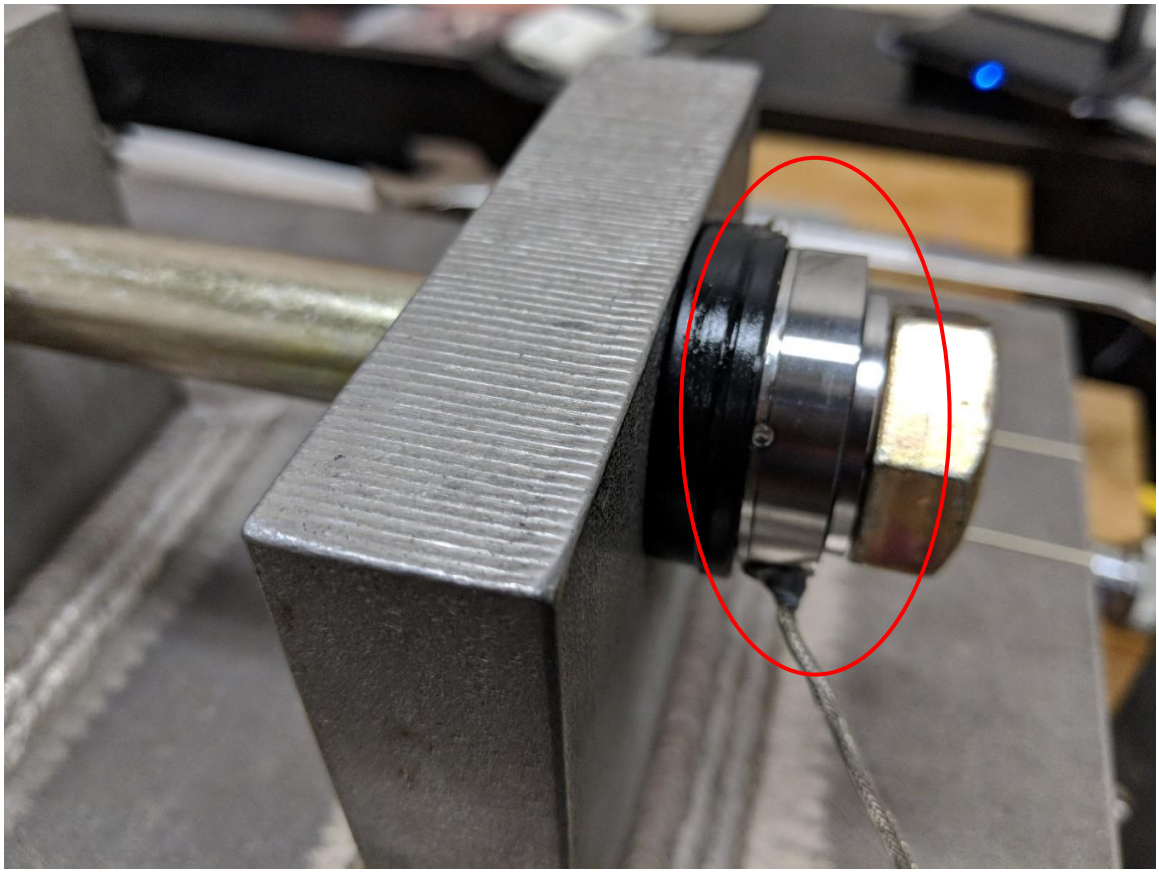

*Figure 3.9: Omega Engineering bolt load cell*

The two load cells were simultaneously calibrated using an MTS uniaxial load frame and an existing 22-kip capacity load cell for reference purposes. During the in-house calibration, the load cells displayed the appearance of operating as intended. In Figure 3.10, the two bolt load cells (S/N, serial number) showed a linear trend of loading versus time with the reference cell. The drop in the curves near the beginning of the calibration is due to slight unloading just before 20 seconds, after which a simultaneous linear trend was observed as the loading increased, before stopping at 20,000 lb.

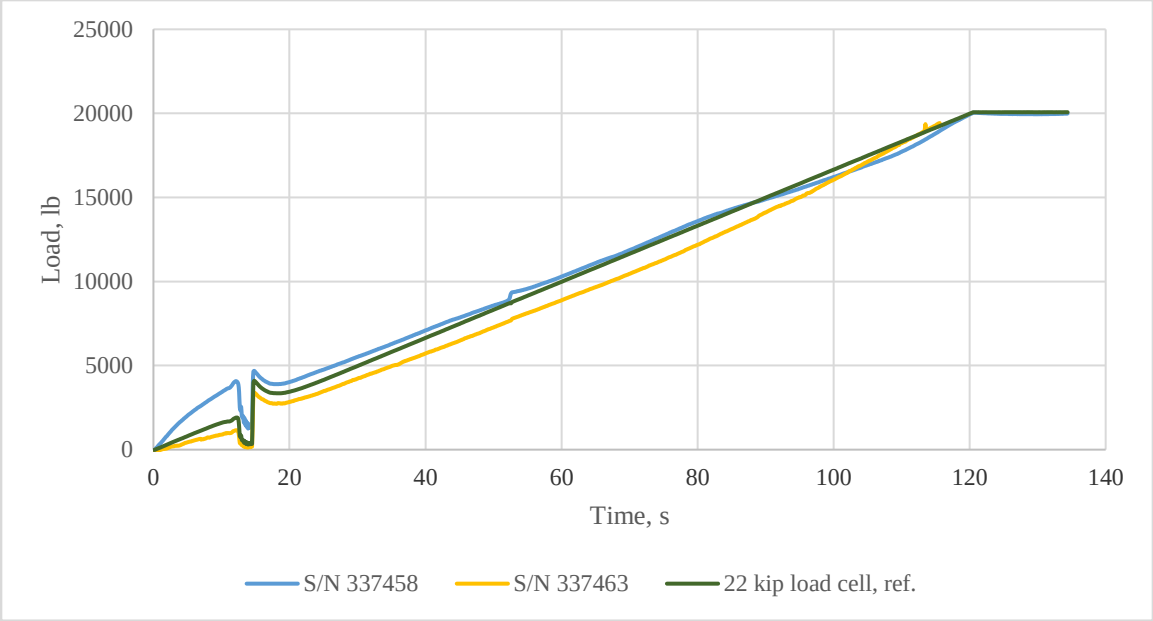


*Figure 3.10: Bolt load cell calibration*

## 3.9 ACOUSTIC EMISSION INSTRUMENTATION AND SETUP

Acoustic emission sensors were used to detect elastic wave events from stress corrosion crack initiation and propagation. The first plate was tested with six WDI-AST wideband differential AE sensors manufactured by Physical Acoustics. The sensors come equipped with a preamplifier and an operating frequency from 100-900 kHz. These sensors allow for a broad range of signals to be detected throughout the testing period. For the second specimen, two R6I-AST AE sensors, which have a higher sensitivity but narrower frequency range of 40-100 kHz, were used in addition to the wideband sensors. The higher sensitivity sensors also come equipped with internal preamplifiers and have an operating frequency of 60 kHz. All sensors were coupled with the stainless-steel plates by way of Hardman structural adhesive epoxy for a secure bond and emission transfer.

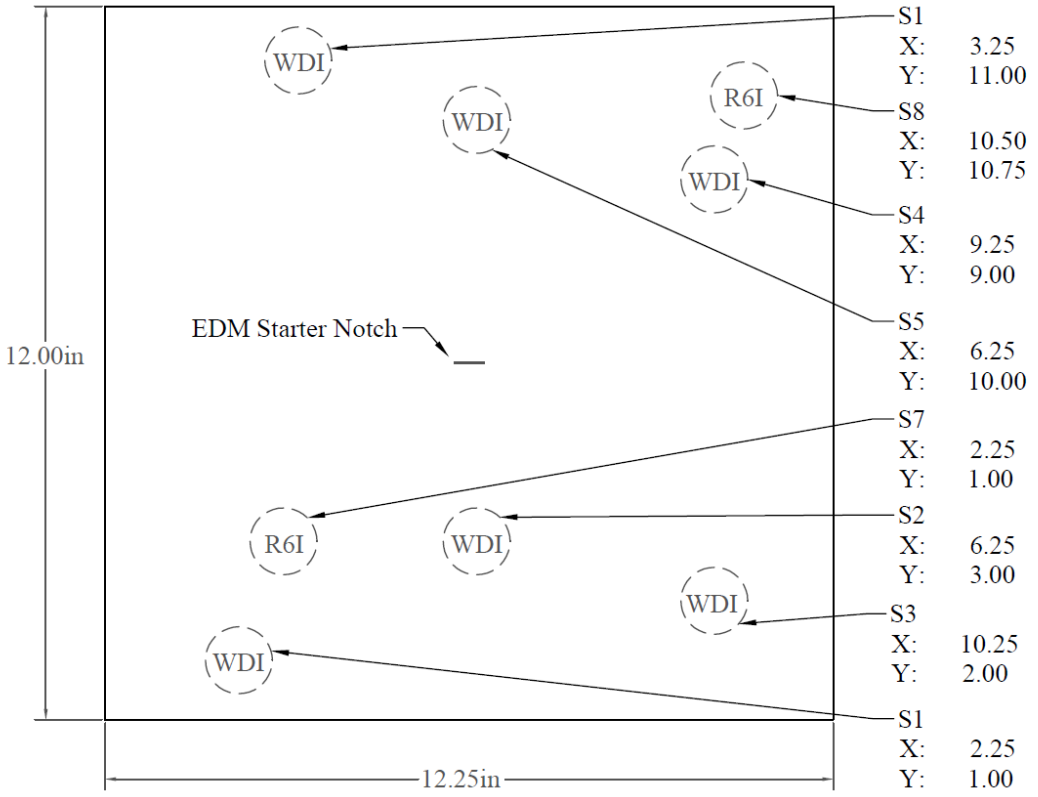


*Figure 3.11: AE sensor attachment schematic for testing*

Locating the specific area of crack initiation and propagation was an important objective. The source location of these events was determined via triangulation of the wave events detected by the sensors. The sensors were arranged on the specimens in a non-symmetrical manner as depicted in Figure 3.11. As noted in the figure, the higher sensitivity (R6I) sensors were not used in the first test (wideband are indicated by WDI). The complete setup for the second test specimen is pictured in Figure 3.12.

The hardware and software used were also manufactured by Physical Acoustics. Data collected from the sensors was obtained using high-speed 4-channel PCI DiSP Advanced DSP workstation cards. This workstation was equipped with four cards for 16 channels of simultaneous data collection. AEWin Real-Time Data Acquisition and Replay

Software was used for feature and waveform processing, displaying the data during testing, data storage, and replay capability.

*Figure 3.12: Testing setup for second plate specimen*

Machine setup is a crucial factor for AE data acquisition. The pre-trigger time, a setting in the software (AEWin) which recovers acoustic waveform prior to crossing the threshold, was set to 256 μs. The sampling rate was set to 1MHz (or 1,000,000 acoustic samples per second). The time from threshold crossing to peak amplitude is called peak definition time and it was set to 200 μs. The hit definition time, which determines when to stop recording a hit and is typically twice the peak definition time, the was set to 400 μs.

Lastly, the hit lockout time, which prevents recording late arriving signals and reflected hits, was set to 200 μs.

## 3.10 SPECIMEN PREPARATION AND PLATE LOADING

The first step of the process was preparing the specimens for testing. Strain gauges were attached to the plates using the manufacturer recommended procedure (Micro-Measurements Bulletin B-137) which utilized M-Bond 200 adhesive. The gauges were placed along the bending axis, so the maximum tensile stress could be monitored. The Omega bolt load cells were installed on the bolt shafts before loading. Both strain gauges and load cell were then connected to a Micro-Measurements P3 Strain Indicator and Recorder.

The most accessible method to load plates bolts was manual operation of a 250 lb-ft capacity torque wrench. Redundancy of loading measurements was used to ensure the plate stayed within the elastic behavior zone of the material (type 304H stainless-steel). If the loading exceeded this target and yielding was experienced, the plate may not behave as anticipated. The specimen might not crack at the starter notch or could crack prematurely in the case of overloading.

All three of these measuring devices (torque wrench, strain gauges, and loadcell) were monitored simultaneously to ensure a proper loading was achieved. The loading values were determined from hand calculations (Appendix A) and used to estimate an equivalent point load created from the bolt tightening. A torque conversion table was also created for use with the torque wrench (Appendix B). A nut-factor of 0.18 was used in the torque calculations due to the lubricated or greased condition of the bolt. The target point loading on the bolt through the welded tabs located at the bottom of the plate was

approximately 6,175 lb. This corresponded to a target wrench torque of 69.40 lb-ft.

The torque wrench and strain readings correlated near the expected target range and thus controlled the stopping point of the loading process. The bolt load cells, however, proved to be unreliable for this testing. They fluctuated readings during loading, and for one of the cells, throughout the duration of testing. The first loadcell was more stable during loading and through testing, but the reading was off target substantially. The reason for the discrepancy in the load cells is likely due to their total capacity of 65,000 lb and having an error of ±3%. Therefore, the relatively low target loading of 6,474 lb could have a substantial variance in acceptable readings (4,550-8,450 lb) according to the load cell specifications.

Six broadband AE sensors (WDI-AST) and two resonant AE sensors (R6I-AST) for each specimen were then attached using epoxy. The monitoring and acquisition software (AEWin) was also prepared for testing. Silicon was used for attaching the solution containment tube and covering the surface of the specimen not in the immediate proximity of the notch (see Figure 3.12).

## 3.11 ASTM E976 PENCIL LEAD BREAK

A pencil lead break test (ASTM E976: Standard Guide for Determining the Reproducibility of Acoustic Emission Sensor Response) was administered on each AE sensor used in the testing to ensure proper response and repeatability. This test also confirms the sensitivity of the sensors and verifies proper coupling of the sensor to the specimen. A mechanical pencil was used to break No. 3 (0.3 mm) graphite lead at an approximate angle of 30° from the horizontal surface of the plate. This procedure was performed five times next to each sensor, as closed to the sensor as possible. The results

are shown in Figure 3.13.

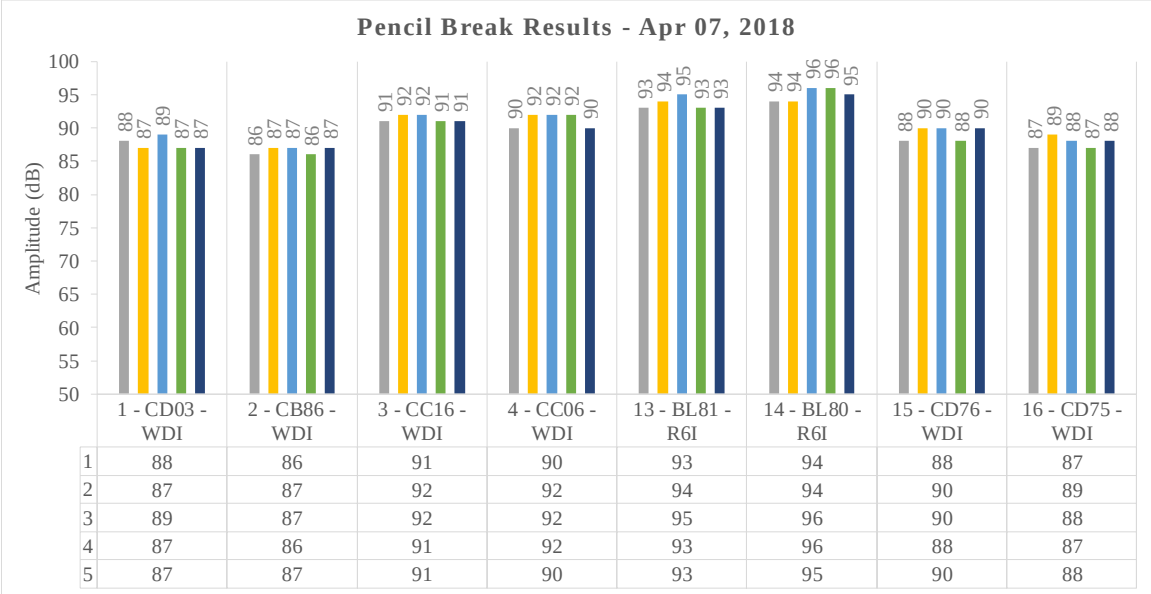


| | 1 - CD03 - WDI | 2 - CB86 - WDI | 3 - CC16 - WDI | 4 - CC06 - WDI | 13 - BL81 - R6I | 14 - BL80 - R6I | 15 - CD76 - WDI | 16 - CD75 - WDI |
|---|---|---|---|---|---|---|---|---|
| 1 | 88 | 86 | 91 | 90 | 93 | 94 | 88 | 87 |
| 2 | 87 | 87 | 92 | 92 | 94 | 94 | 90 | 89 |
| 3 | 89 | 87 | 92 | 92 | 95 | 96 | 90 | 88 |
| 4 | 87 | 86 | 91 | 92 | 93 | 96 | 88 | 87 |
| 5 | 87 | 87 | 91 | 90 | 93 | 95 | 90 | 88 |

*Figure 3.13: ASTM E976 - pencil lead break results for plate 2*

All wideband sensors showed responses with variation of 3 dB or less through their respective pencil break test. The lowest and highest response within the entire wideband group varied by only 6 dB. Likewise, the resonant sensors showed a difference in response of only 3 dB per sensor and 4 dB difference within the group. These outcomes show an acceptable level of response and repeatability for the duration of testing. Earlier pencil lead break tests that resulted in variations greater than that shown above were rejected and repeated after adjusting the sensor, epoxy, cable, channel, or a combination of these.

## 3.12 MATERIAL VELOCITY DETERMINATION

Once the data from the pencil lead break was obtained, the experimental velocity in the respective plates could be determined using the difference in time of event response in the sensors and their attachment distance with respect to one another. For a pencil lead break at each sensor, the wave velocity was determined at the five remaining sensors. This

was repeated for all sensors and average experimental pressure wave speed velocities were determined, see Table 2.

*Table 3.1: Average wave velocity for individual plate specimens*

| Average Wavespeed | | |
|---|---|---|
| Plate #1 | 235,900 | in/s |
| | 19,660 | ft/s |
| | 5,993 | m/s |
| Plate #2 | 227,100 | in/s |
| | 18,920 | ft/s |
| | 5,769 | m/s |

# CHAPTER 4. RESULTS AND DISCUSSION

## 4.1 VISUAL DISCOLORATION OF EXPOSED SURFACE

A slight discoloration of the metal was evident from early in testing after first exposure to the solution. However, this change only tinted the surface of the stainless-steel a few shades darker. A more drastic change in color was noted after visible cracking had occurred in the plate. Photographic evidence of this phenomenon is provided during days 0, 6, and 19, in Figure 4.1.

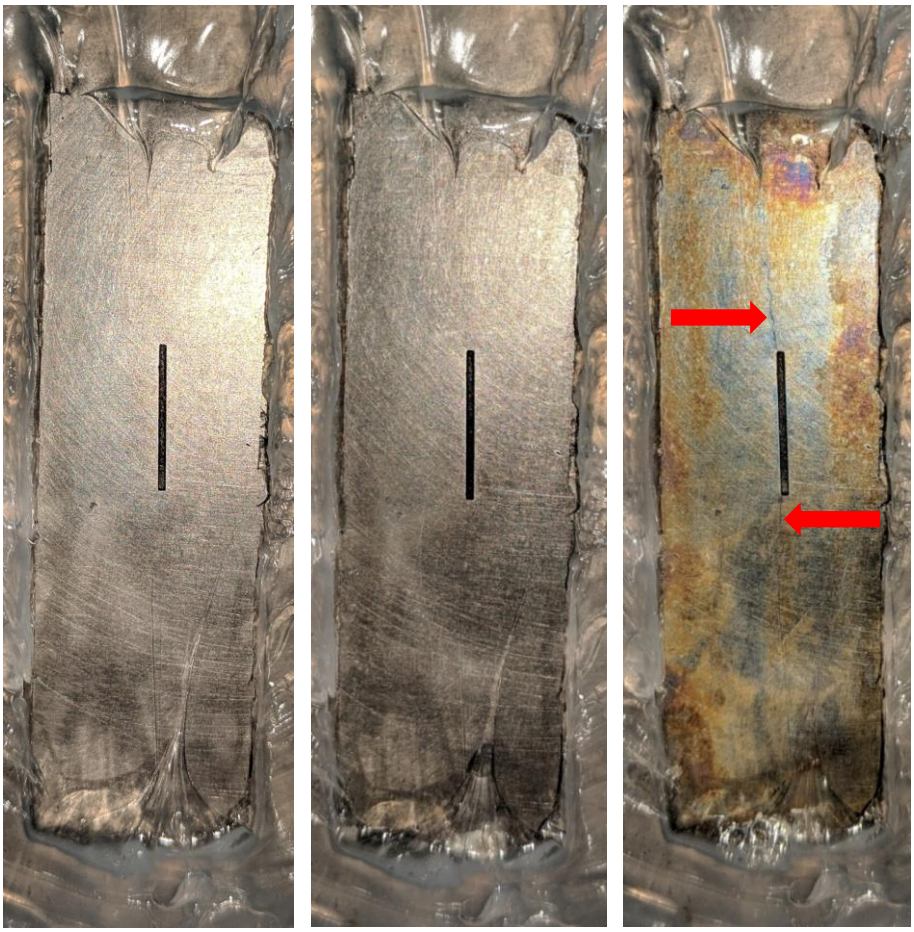

*Figure 4.1: Photos of the solution exposed specimen at day 0, day 6, and day 19*

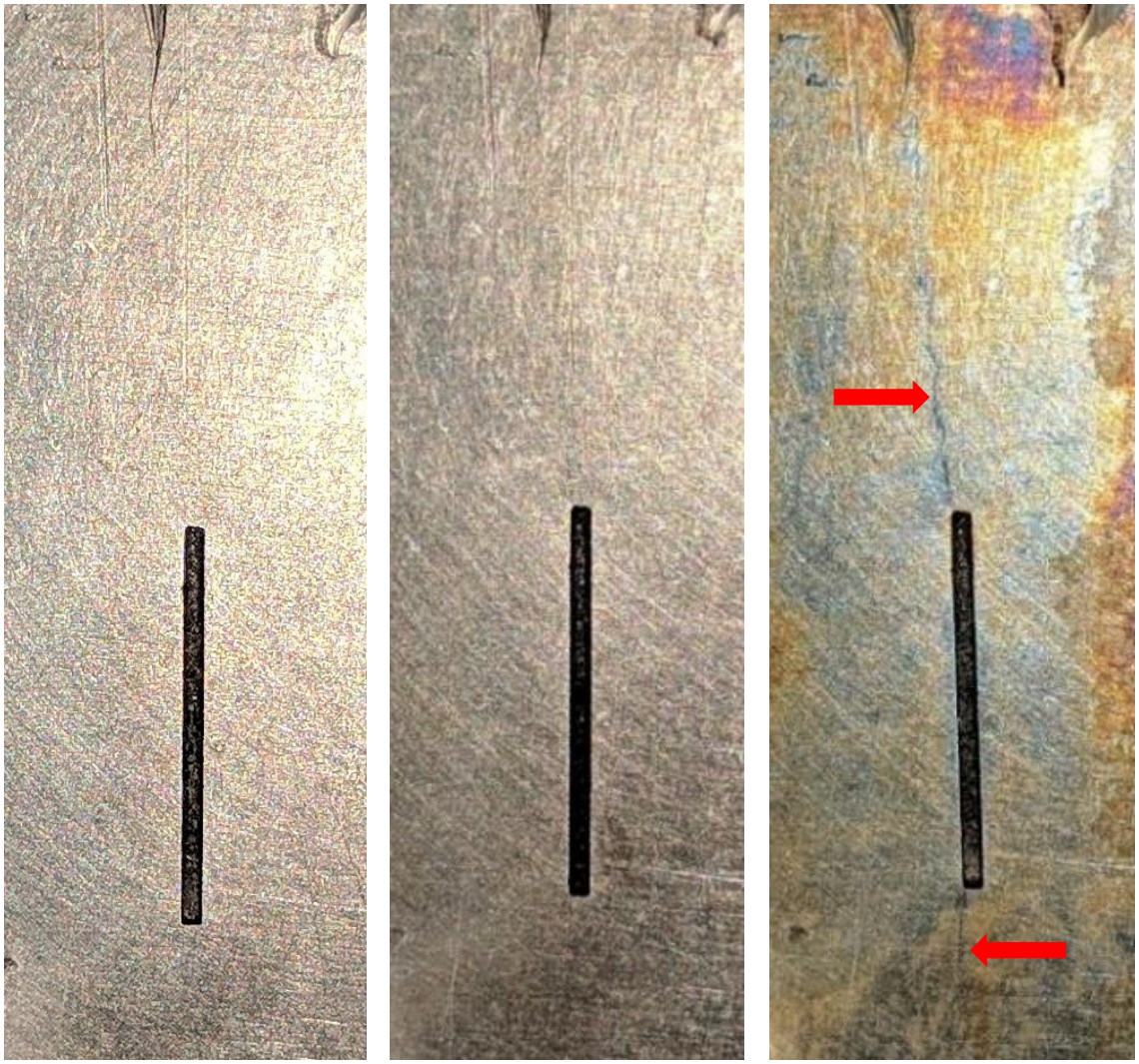

*Figure 4.2: Photos of the notch at day 0, day 6, and day 19 of testing*

Figure 4.2 is similar to the previous, but at greater magnification. The sample appearance before any solution was applied (left), was a slightly lighter shade than after 6 days (center), but this change was hardly distinguishable by photo. Until cracking was detectable, the samples did not show drastic change in visible discoloration of the material surface. Conversely, it was obvious when a sizable crack opened from the amount of oxidization present within the sample area. This change had occurred within the space of 1-to-2 days, maximum. The sudden release of rust-colored oxidation potentially correlates

with the opening movement or propagation of the crack from the EDM notch (visible in the figure). A faint hairline fracture extending from the top and bottom of the notch is plainly visible in the right image. The total length of visible crack propagation was measured to be approximately 0.75 inches from each end of the starter notch. In this example, cracking may have already taken place at the top of the notch in the left image. Slight fracturing may be visible at the top of the notch in the middle image, but no cracking was noted at the bottom of the notch.

## 4.2 DATA PROCESSING AND ANALYZATION

Once cracking was visually noted through the notch of the plate, analyzing the AE data could commence with the goal of locating acoustic emissions related to crack initiation and propagation. Figure 4.3 below shows the raw data captured by the AEWin software. This plot shows AE hit amplitude recorded over the entire testing period.

Amplitude is defined as the greatest voltage in a waveform and is measured in decibels (dB). Decibel is the preferred unit of measure for AE data collection and analyzation. Like many types of sensors, AE sensors produce feedback in voltage when the piezoelectric element within is excited. A conversion from voltage to decibel is therefore necessary. This can be achieved using equation 11.

$$A = 20 * log_{10} \frac{V}{V_0} * dB \qquad \text{(eq. 11)}$$

where,

$A$ = Amplitude ($dB$)
$V$ = Voltage ($V$)
$V_0$ = Reference Voltage (1 V)

The only filter used on the data shown in the figure was an amplitude threshold set

at 32 dB. Everything below the threshold was rejected by the software in the acquisition phase.

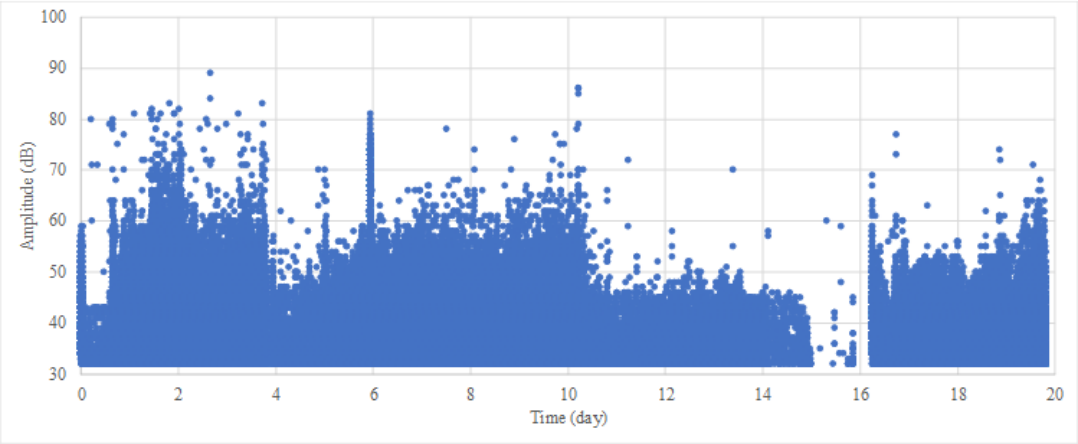


*Figure 4.3: Raw acoustic emission data acquired during testing by AEWin software, amplitude vs. time*

To better understand the data distribution with respect to the individual sensors, it was further separated into isolated plots: all wideband, all resonant, and then individual sensors (Figures 4.4-4.13). Figure 4.4 displays the collective wideband data and Figures 4.5-4.10 show the individual wideband sensor data (sensors S1-S6). Figure 4.11 displays all resonant data followed by Figures 4.12 and 4.13 for the individual resonant sensors (sensors S7 and S8).

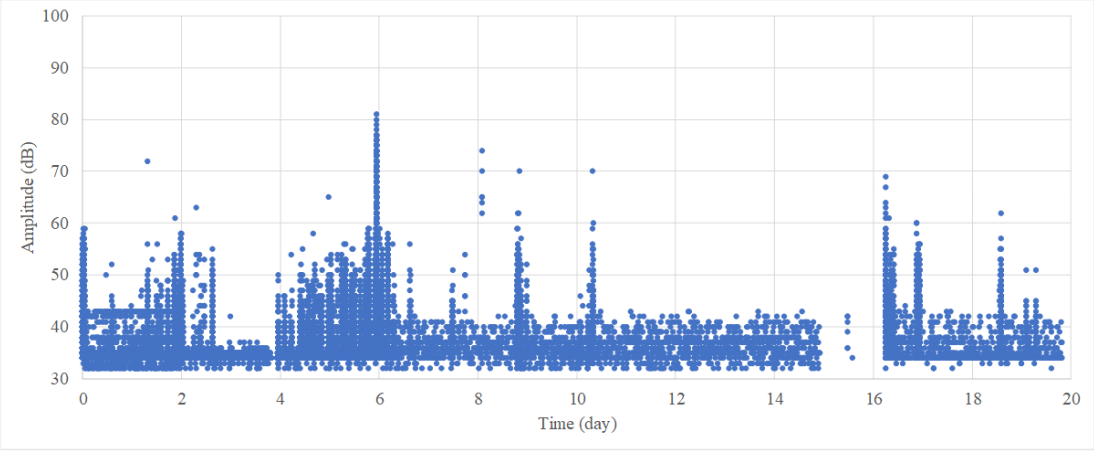


*Figure 4.4: Collective wideband raw data, amplitude vs. time*

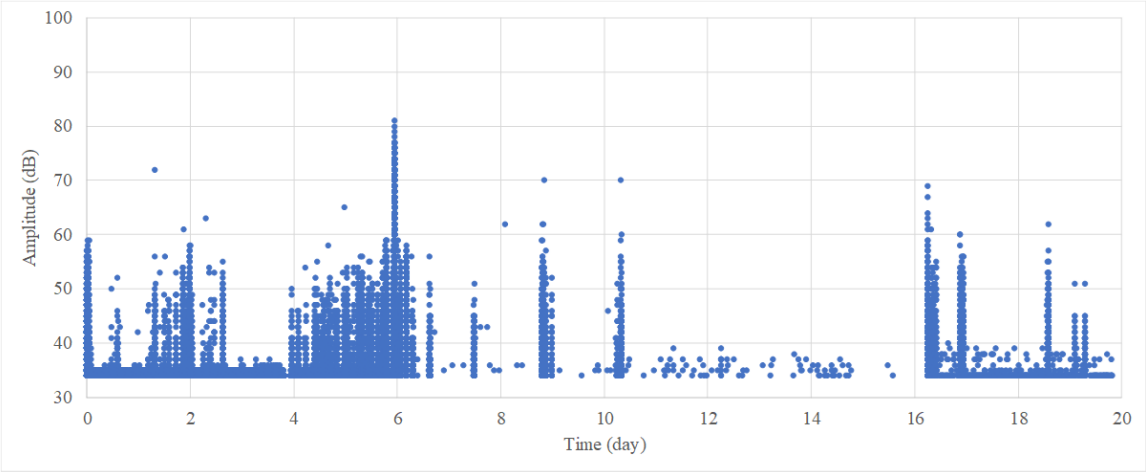


*Figure 4.5: Wideband raw data for sensor S1, amplitude vs. time*

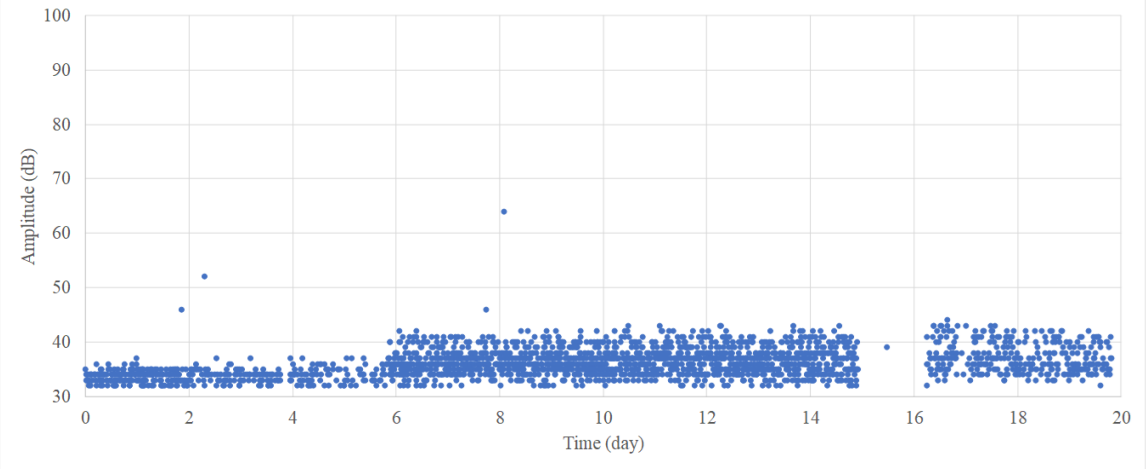


*Figure 4.6: Wideband raw data for sensor S2, amplitude vs. time*

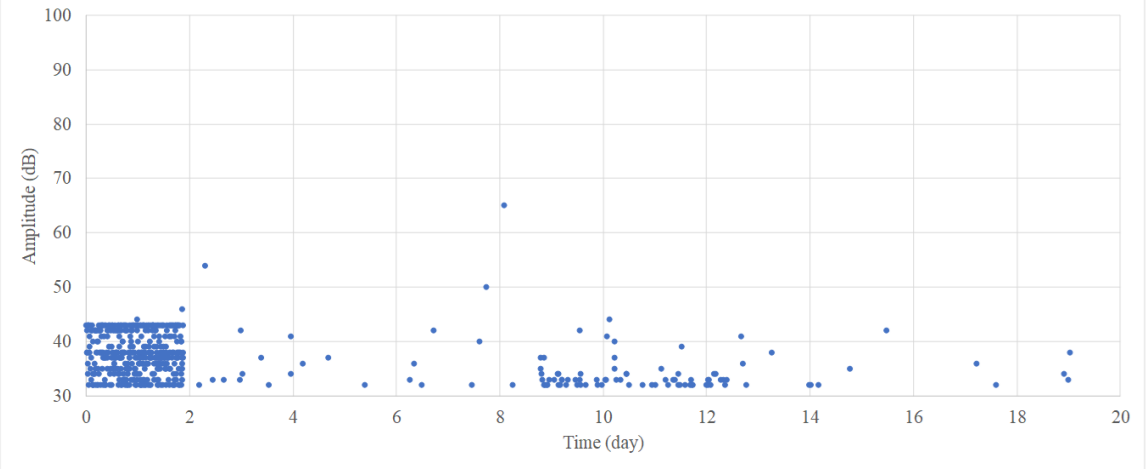


*Figure 4.7: Wideband raw data for sensor S3, amplitude vs. time*

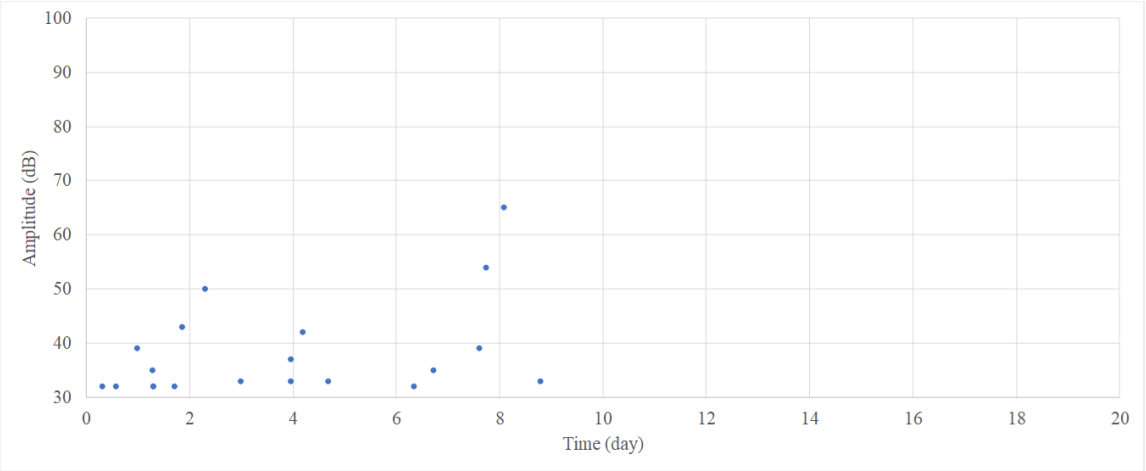


*Figure 4.8: Wideband raw data for sensor S4, amplitude vs. time*

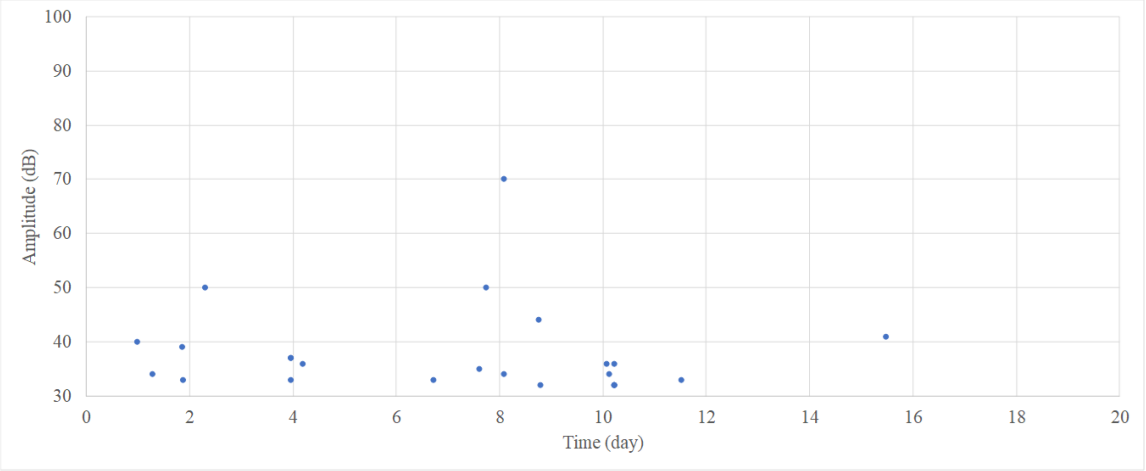


*Figure 4.9: Wideband raw data for sensor S5, amplitude vs. time*

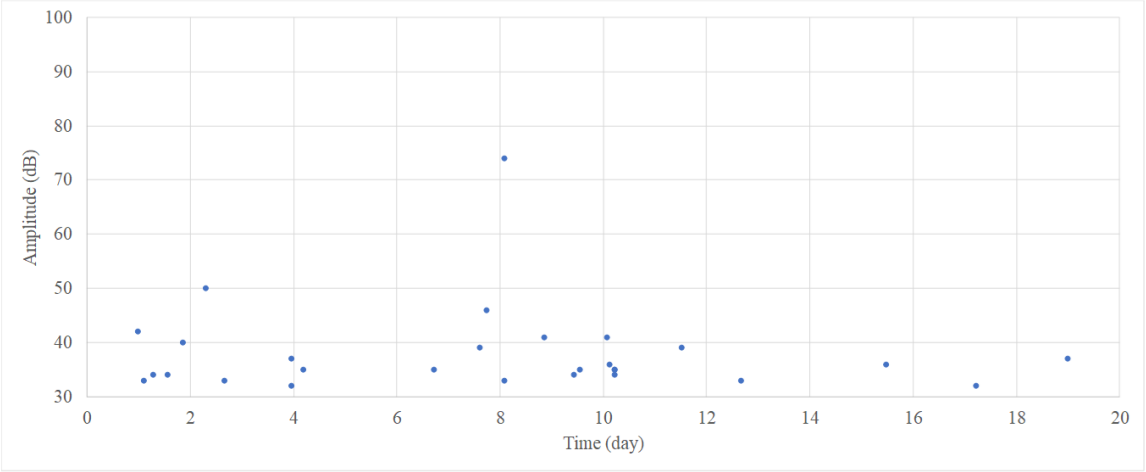


*Figure 4.10: Wideband raw data for sensor S6, amplitude vs. time*

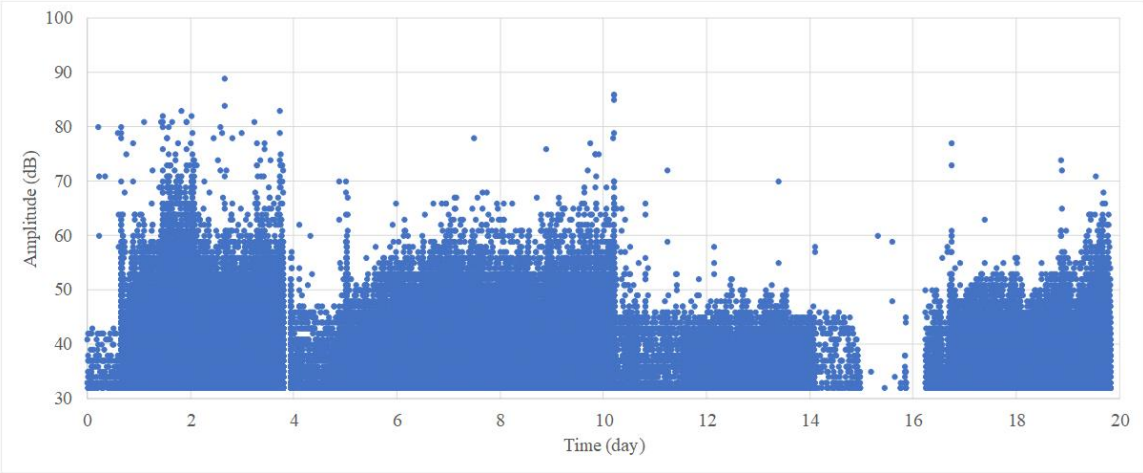


*Figure 4.11: Collective resonant raw data, amplitude vs. time*

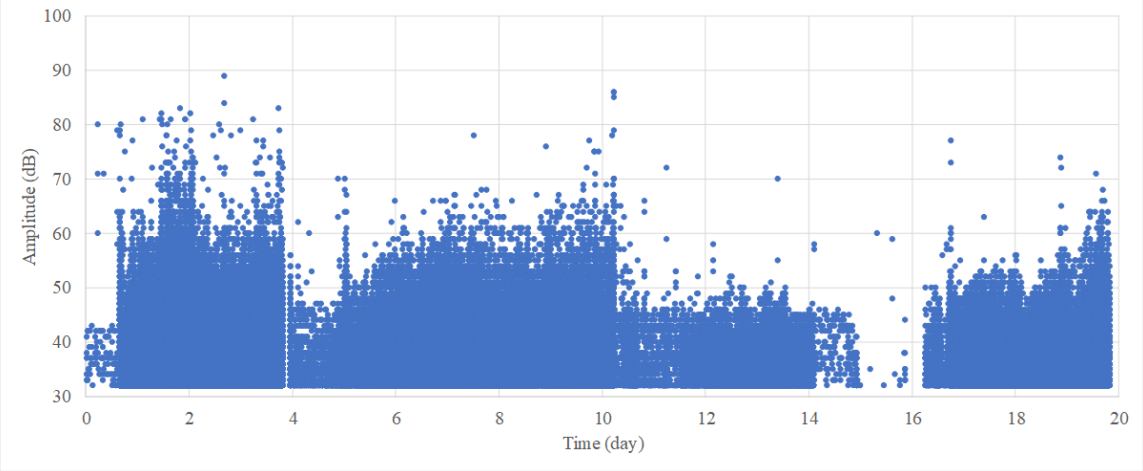


*Figure 4.12: Resonant raw data for sensor S7, amplitude vs. time*

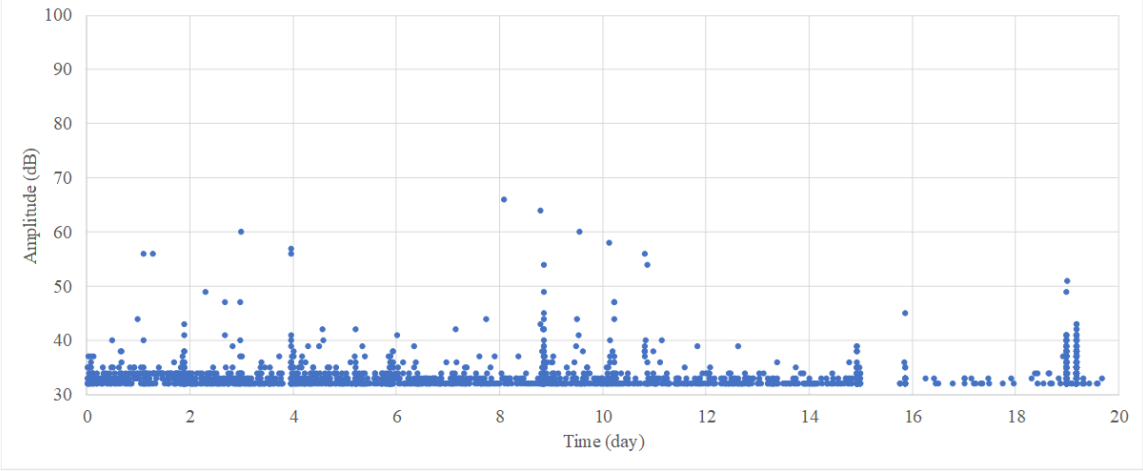


*Figure 4.13: Resonant raw data for sensor S8, amplitude vs. time*

Except for sensor S1, S2, and the first two days for S3, the wideband sensor data appeared to be largely genuine from initial visual inspection of the waveforms. The resonant data, particularly from sensor S7, accounted for the bulk of the sample. Many of the emissions from these sensors appeared to be suspicious based on visual inspection of waveforms. Figure 4.14 provides examples of waveforms having characteristics of genuine data (left), and waveforms that are suspected to be from noise (right).

The data was filtered using AEWin and NOESIS software to minimize extraneous data. These extraneous hits are generally not related to genuine cracking emissions and can be caused by a variety of sources, including faulty cables or connections. Some of the sensors were detecting noise at higher amplitudes than others and were adjusted to a higher threshold accordingly. An example of this setup modification occurred with sensor S3, where extraneous data was observed during early testing and then corrected near day 2. Other extraneous emissions, within sensor S1 and S2 for example, were not as easily correctable and filtered after data collection by manually deleting data that was visually distinguishable by waveform (Figure 4.14).

Once the extraneous data was removed from the raw wideband data, a more realistic representation of genuine emissions from the tensile stress cracking remained, see Figure 4.15. The figure is color coded by sensor.

Suspected crack initiation and/or propagation events begin to appear in the figures where multiple sensors respond to the event at nearly identical times with respect to the total test duration. In the figure, these events occur at a higher amplitude than the other hits closer to the threshold. When a crack event occurs, the sensor closest to the crack is

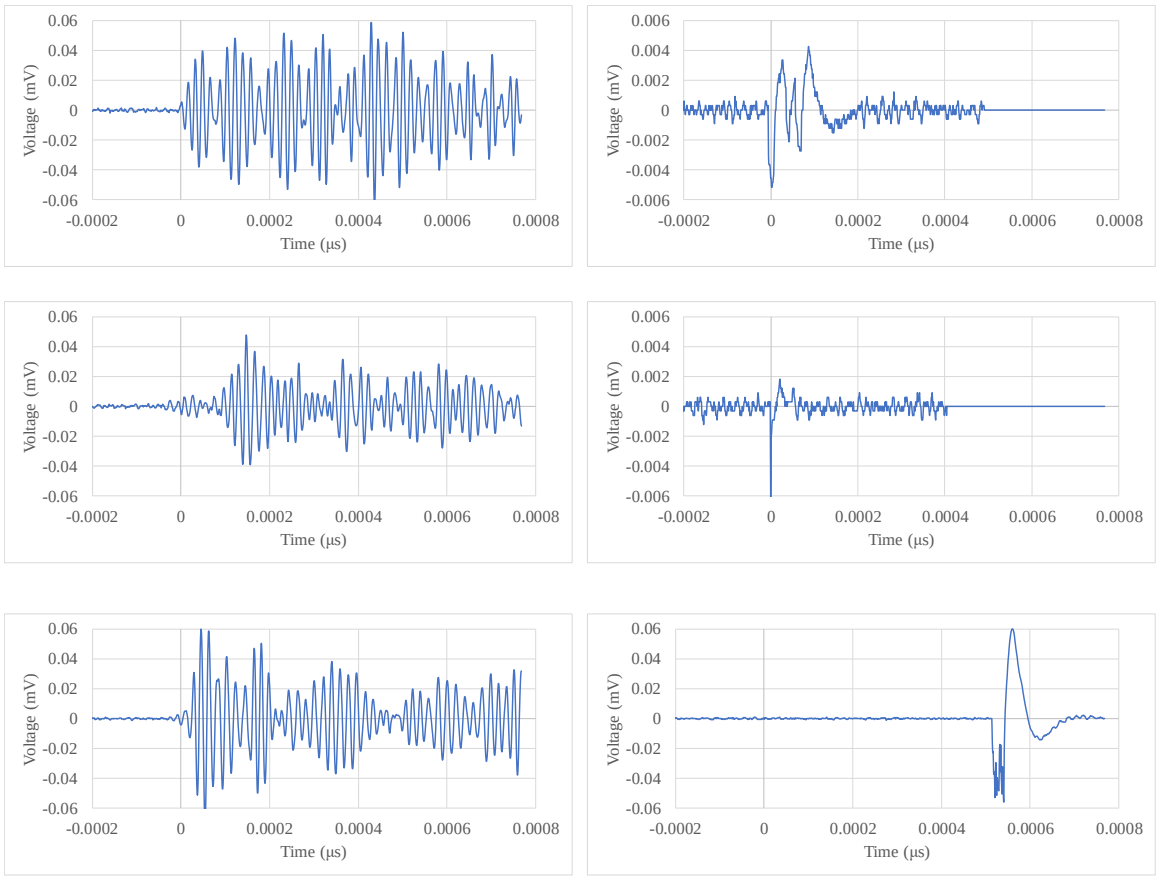


*Figure 4.14: Examples of genuine and suspicious (resonant) waveforms*

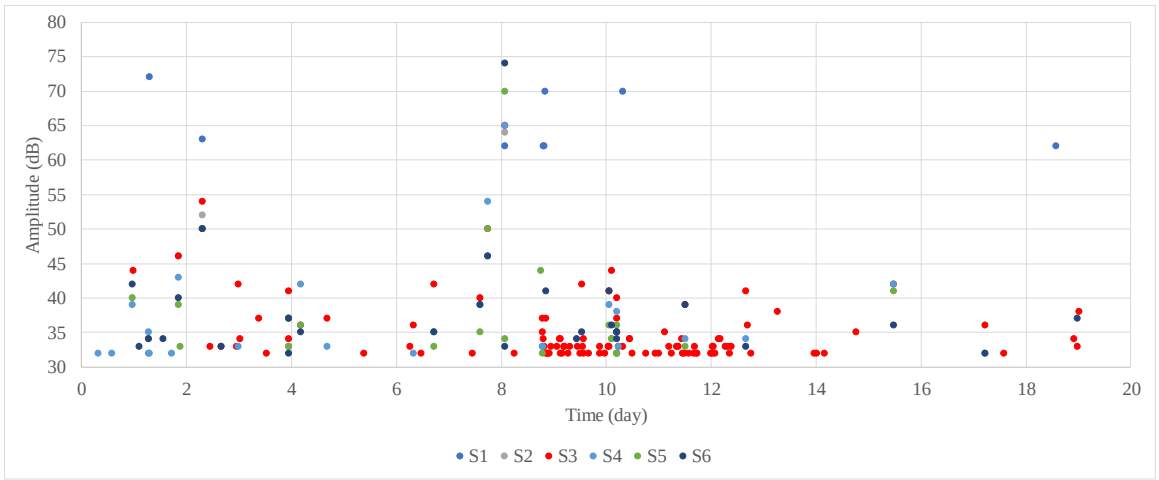


*Figure 4.15: Filtered wideband data, amplitude vs. time*

expected to respond with the highest decibel amplitude. The signal will dissipate as the wave propagates through the medium and sensors further from the source will generally

detect at lower amplitudes. This behavior can be viewed within the plot as the hits appear to form vertical lines on the scatter plot. Other acoustic activity at lower decibels could potentially be attributed to corrosion activity, microcracking, or noise.

Signal strength and duration are other useful indicators of acoustic activity related to cracking in materials. Therefore, they can also be utilized to gain a better idea of what is happening during testing. In this case, Figure 4.16 shows the cumulative signal strength of all recorded hits (solid line) throughout testing overlaid with amplitude. The strength of an acoustic emission hit is calculated by the area under the waveform signal envelope as measured by the sensor output voltage (units in pico volt seconds, pVs). Similarly, Figure 4.17 contains the same cumulative signal strength, but amplitude is replaced with event duration. Duration refers to an AE feature that represents the time difference of a hit, as it first crosses the threshold, and terminating when it last crosses (units in micro-seconds, μs).

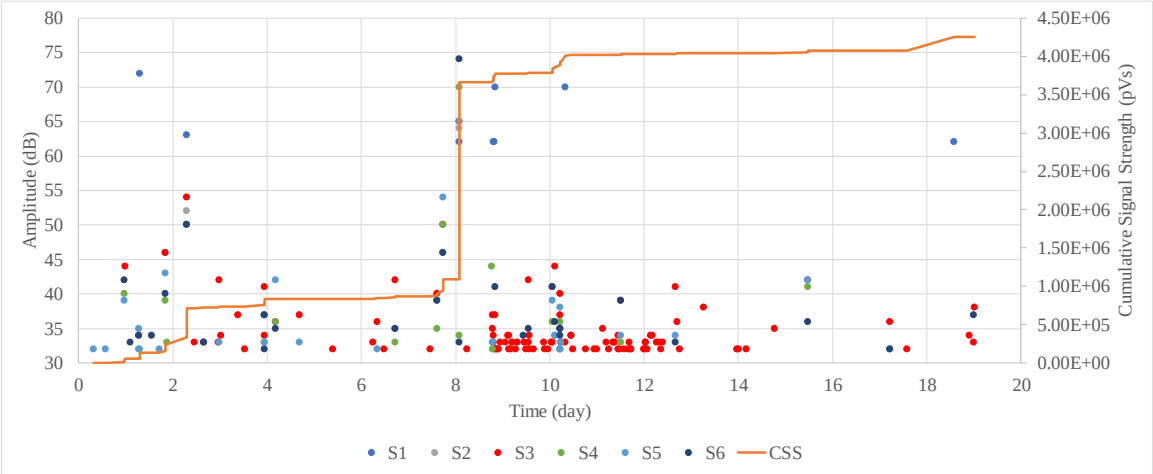


*Figure 4.16: Filtered wideband data, amplitude and cumulative signal strength vs. time*

In these figures, the events captured with multiple sensors in very short time periods have a corresponding jump in the signal strength as each successive event is occurring.

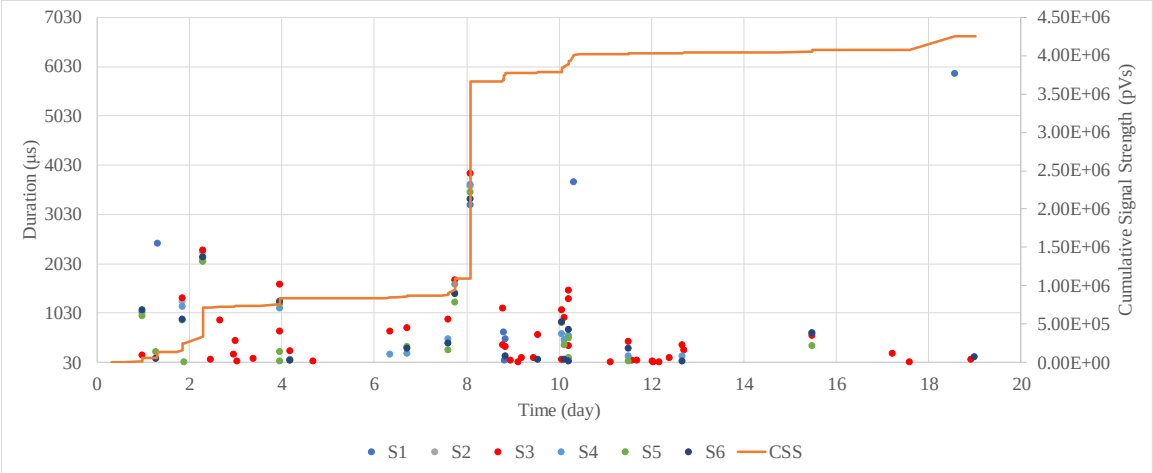


*Figure 4.17: Filtered wideband data, duration and cumulative signal strength vs. time*

These "steps" in the cumulative signal strength curve likely correspond to a new cracking event or propagation along an existing crack. Likewise, the hits where increases in signal strength occur, also show greater time duration than the other hits.

Due to the substantial amount of extraneous data within the more sensitive resonant data, a similar filtering procedure could not be followed. Analyzing the waveform features proved to be the most effective method for filtering the resonant data. A threshold of 35 dB was used for sensors S8 and S7, which eliminated some of the noise. Hit count, signal strength and duration were also used to filter much of the data collected from these sensors. The hit count is the number of times the acoustic emission signal exceeded the threshold during the testing period. Based on visual inspection of the data, emission counts of 10 or less were removed from the data set. Signal strength and duration, discussed earlier in this section, were set to filter any emissions less than 10,000 pVs and 10 µs, respectively (this eliminated tens-of-thousands of hits). After these filters were applied some extraneous data remained. Further manual filtering, by way of analyzing the individual waveforms, was performed thereafter. The waveform examples in figure 4.14 are actual hits acquired from the resonant sensors extracted during this process. The resonant amplitude versus

time plot is provided in Figure 4.18.

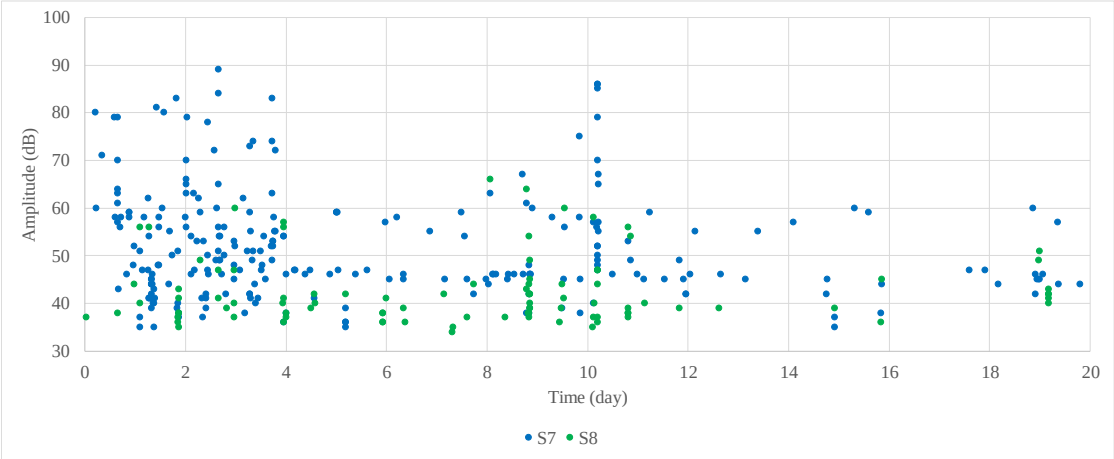


*Figure 4.18: Filtered resonant data, amplitude vs. time*

Per the procedure discussed, relating to the wideband sensors, incorporating the cumulative signal strength should indicate when significant hits (perhaps relating to cracking) may be taking place. The steps in the cumulative signal strength within Figure 4.19 are similar in quantity to the wideband, and the initial steps occur after day two, but the second major step in signal strength happens later in the resonant plot. Therefore, one cracking event likely occurring around day two, and a second potential major event near day 10.

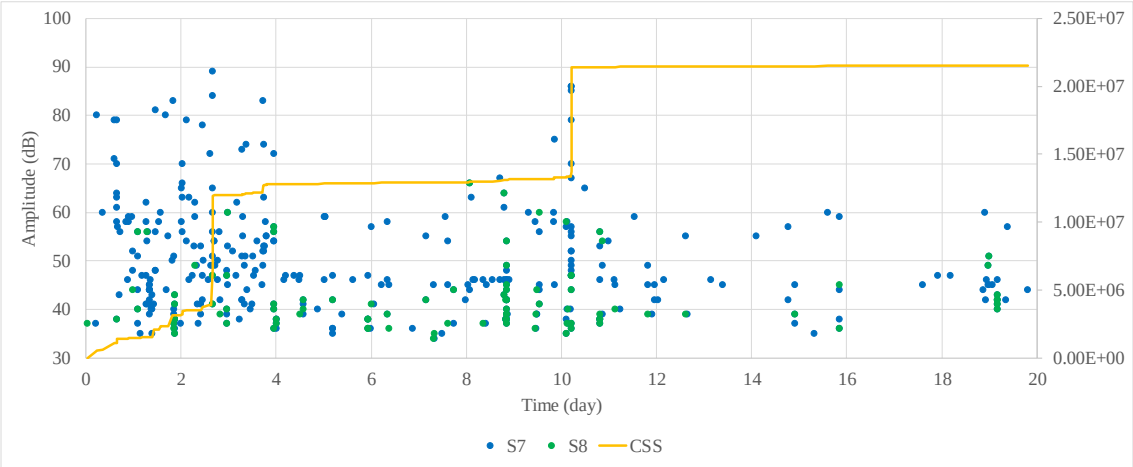


*Figure 4.19: Filtered resonant data, amplitude and cumulative signal strength vs. time*

The collective filtered data from all sensors is shown in Figure 4.20. Within this plot, the events of interest near days two and eight for the wideband plot (Figure 4.15), are now more pronounced with hits from all sensors on the plate. However, the event near day two is now somewhat obscured by the resonant data.

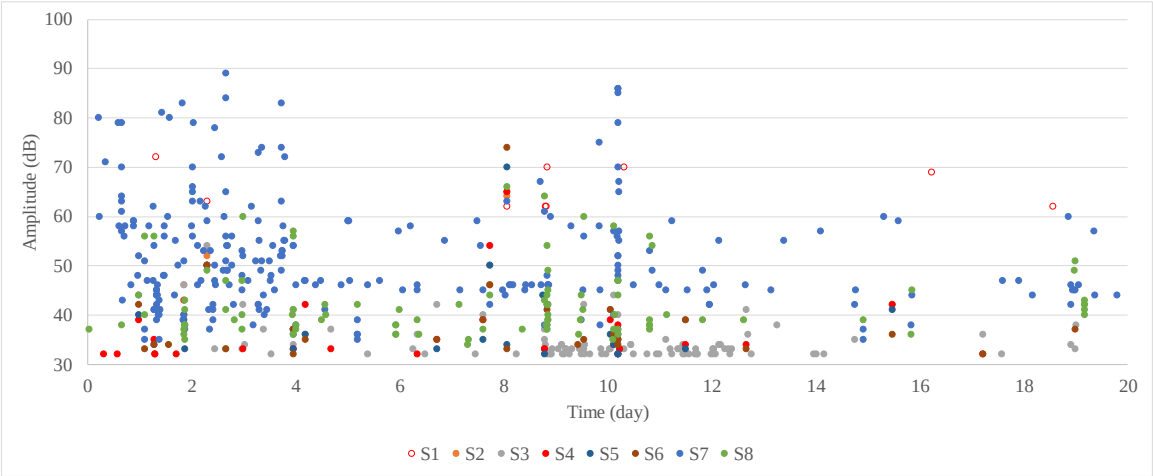


*Figure 4.20: Complete filtered data, amplitude vs. time*

Once the all filtered data is combined with signal strength, a more complete picture can be observed (Figure 4.21). Signal strength steps up at similar times, but it is less pronounced than with either wideband or resonant data alone. This is potentially indicative of cracking and micro-cracking taking place in the plate.

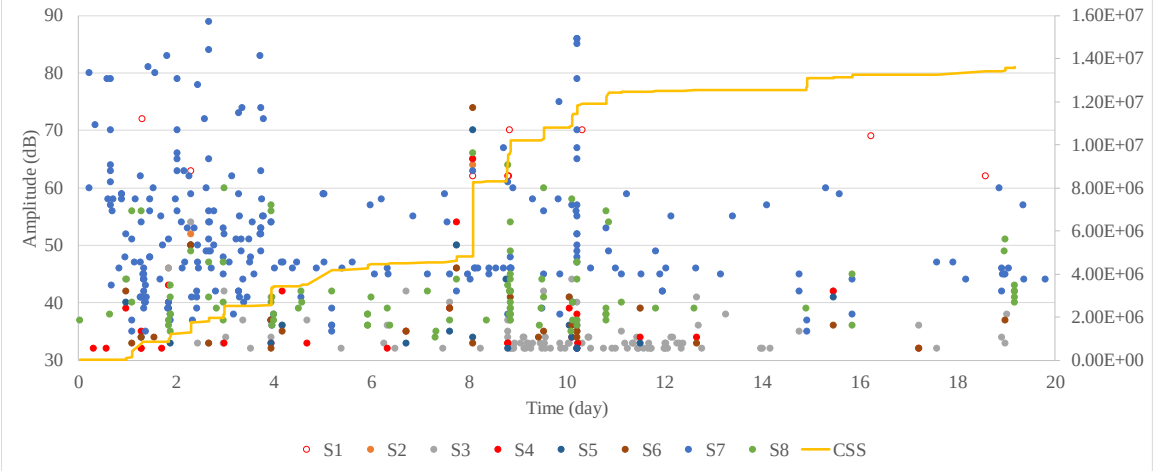


*Figure 4.21: Complete filtered data, amplitude and cumulative signal strength vs. time*

When comparing a plot showing amplitude versus time (Figure 4.20 or 4.21), and one with signal strength versus time (Figure 4.22), three significant events are further detailed. One occurs just after the two-day mark, another before the eight-day mark, and the last, nearly at the eight-day mark. In the signal strength plot, there are noticeable events where many sensors respond to a single emission.

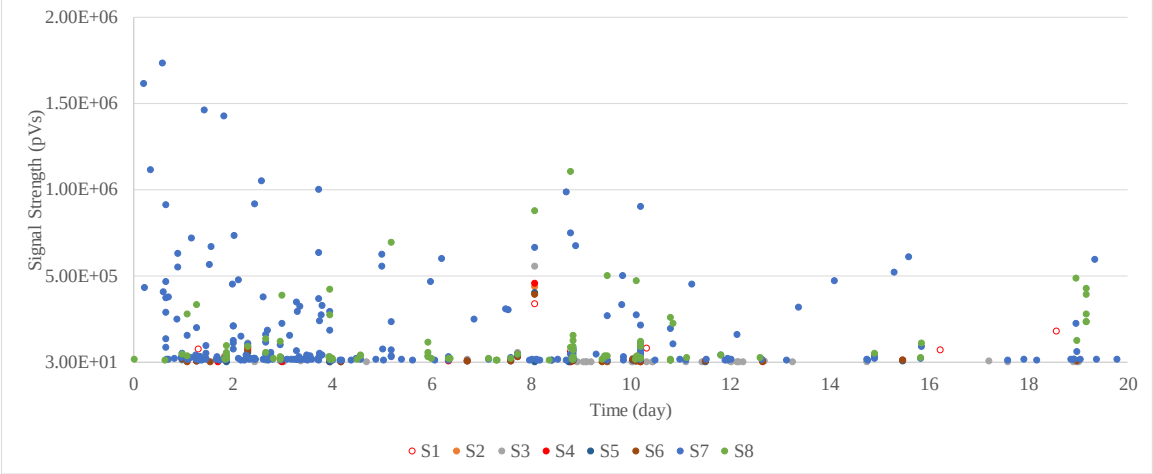


*Figure 4.22: Complete filtered data, signal strength vs. time*

Another tool used in identification of AE events is source location, or the practice of locating an event occurrence within the specimen. This is achieved through triangulation of three or more sensors, utilizing the location of the sensors relative to the plate, and the wave velocity through the material. The velocity was determined by way of the data obtained from ASTM pencil break tests (ASTM E976 and ASTM E1316) discussed earlier in this chapter, and the placement of the sensors on the specimen.

The acquisition software (AEWin) has built-in features for source location, using the inputs of sensor coordinates and experimentally obtained wave velocity, to locate potential events of significance. As discussed, these events possess hits from multiple sensors with significant decibel amplitude, duration, and signal strength.

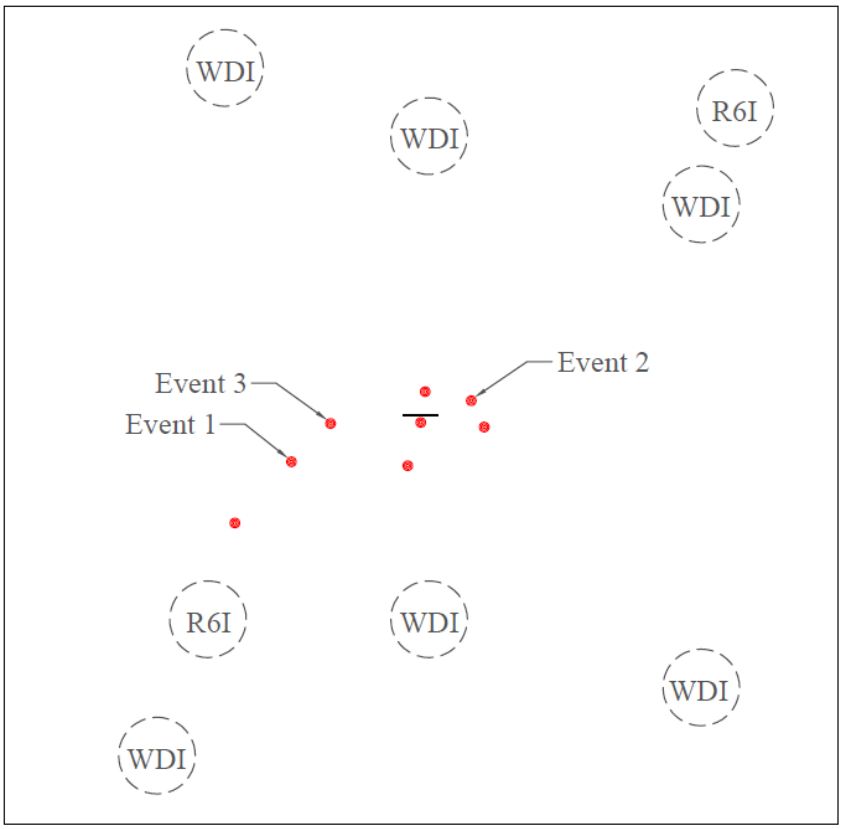


*Figure 4.23: Source location results diagram from plate test number 2*

The red dots scattered around the plate notch in Figure 4.23 represent events with multiple sensor hits from the testing data. The events are numbered chronologically. Also shown in the figure are the sensor locations labeled with their type (wideband WDI or resonant R6I) and the location of the EDM starter notch.

Some of the events were located near identifiable cracking events while others were not as obvious. Furthermore, some did not show significant characteristics likely related to cracking. The events labeled in the Figure, Events 1, 2, and 3, did have favorable AE features and are located near the notch cracks. They are detailed in the following text due to their significant decibel amplitude, signal strength, and waveform characteristics.

Figure 4.24 shows the location of these events and their respective time of occurrence during testing.

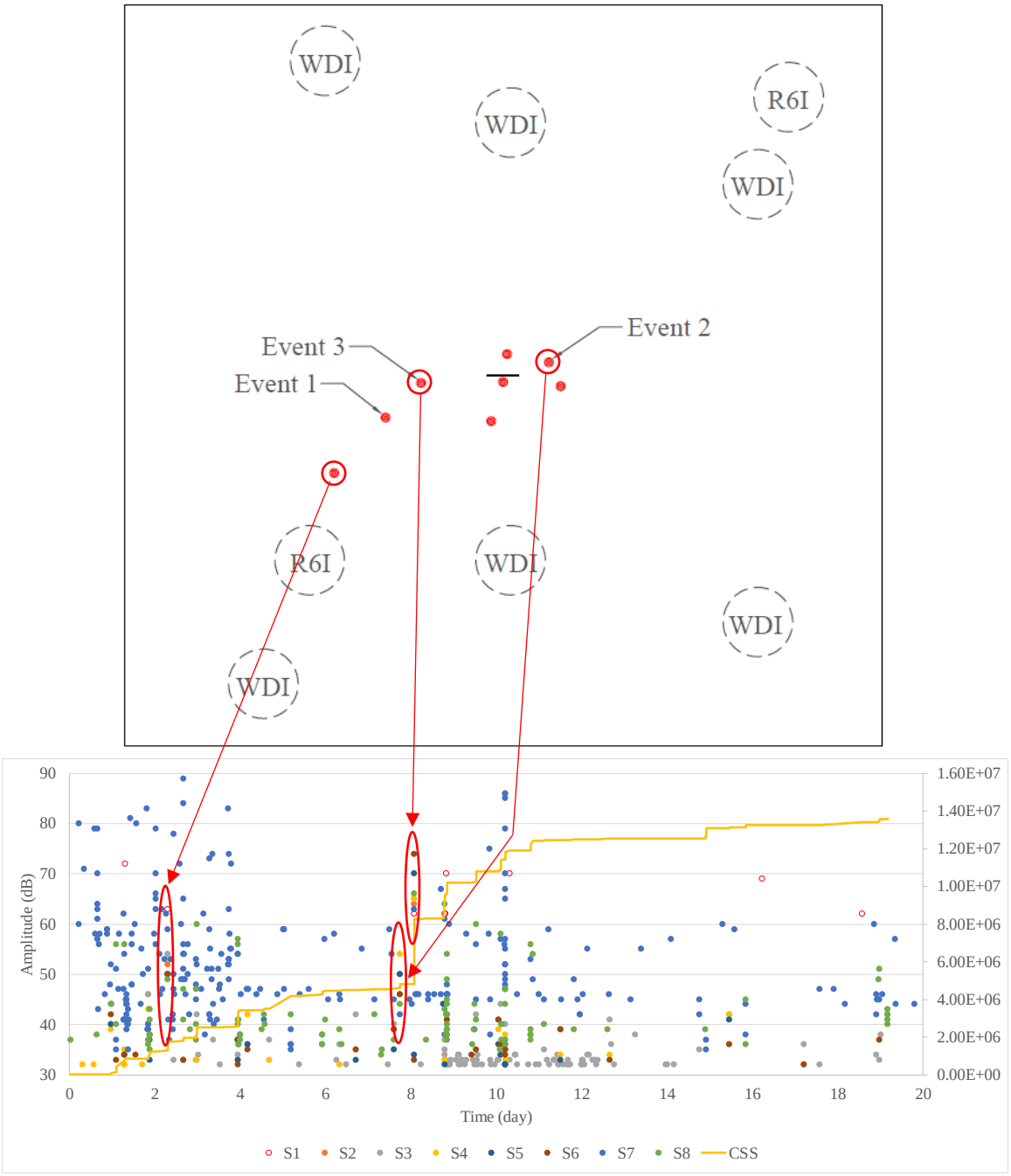


*Figure 4.24: Linking significant events from source location to their time of occurrence*

The next step involved breaking these three events down and observing how they propagated through the stainless-steel plate. This was achieved by analyzing the individual wave travel time to each sensor and the order of sensor hits from the perspective of the event origin (Figures 4.25-4.27).

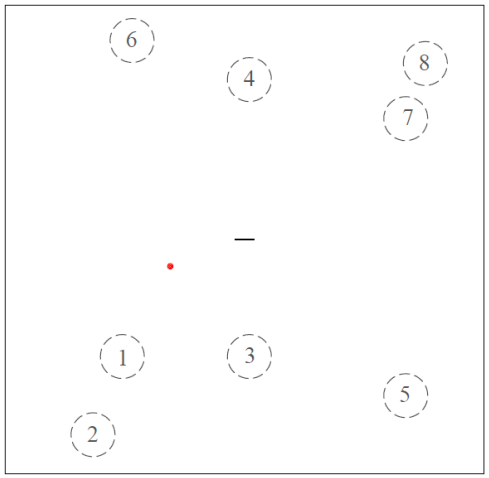


| Event 1 | | |
|---|---|---|
| **Order Received** | **AE Sensor** | **Time to Sensor (µs)** |
| 1 | S7 - R6I | 0 |
| 2 | S1 - WDI | 11.5 |
| 3 | S2 - WDI | 17.5 |
| 4 | S5 - WDI | 53.5 |
| 5 | S3 - WDI | 54.2 |
| 6 | S6 - WDI | 64.7 |
| 7 | S4 - WDI | 67.2 |
| 8 | S8 - R6I | 78.5 |

*Figure 4.25: Event 1 order of response, corresponding sensor, and time to sensor*

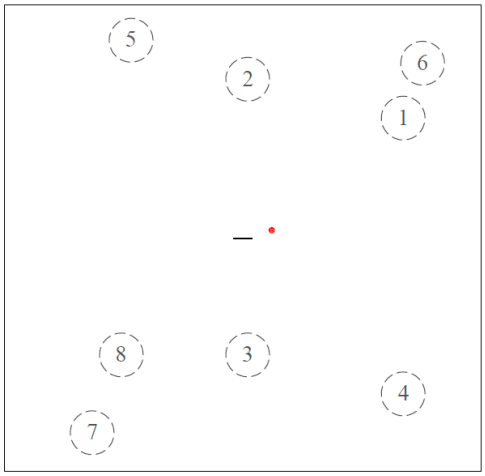


| Event 2 | | |
|---|---|---|
| **Order Received** | **AE Sensor** | **Time to Sensor (µs)** |
| 1 | S4 - WDI | 0 |
| 2 | S5 - WDI | 1.5 |
| 3 | S2 - WDI | 22.5 |
| 4 | S3 - WDI | 22.7 |
| 5 | S6 - WDI | 33.3 |
| 6 | S8 - R6I | 34.5 |
| 7 | S1 - WDI | 74.2 |
| 8 | S7 - R6I | 79.5 |

*Figure 4.26: Event 2 order of response, corresponding sensor, and time to sensor*

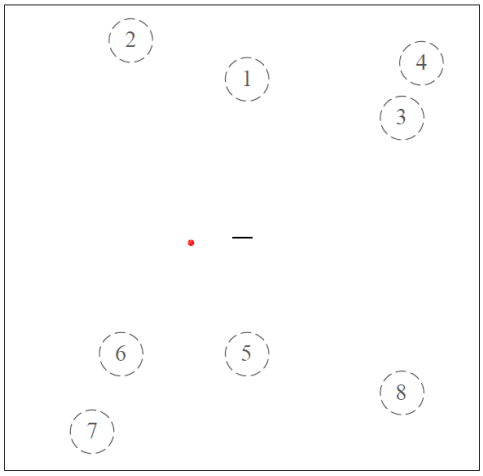


| Event 3 | | |
|---|---|---|
| **Order Received** | **AE Sensor** | **Time to Sensor (µs)** |
| 1 | S5 - WDI | 0 |
| 2 | S6 - WDI | 3.0 |
| 3 | S4 - WDI | 14.0 |
| 4 | S8 - R6I | 23.7 |
| 5 | S2 - WDI | 27.0 |
| 6 | S7 - R6I | 28.3 |
| 7 | S1 - WDI | 40.0 |
| 8 | S3 - WDI | 41.0 |

*Figure 4.27: Event 3 order of response, corresponding sensor, and time to sensor*

For each event, the order of responding sensor signals agrees from the perspective of a wave propagating outward from the origin of a crack beginning at the starter notch. The time of response from the event location shows a similar order of magnitude (in μs) for all three sample events. Response time and order received is consistent throughout the events respective to the origin location, except for the resonant sensors (sensor S7 and S8) in event 2. This may be attributed to the differing sensitivity of the resonant and wideband sensors.

## 4.3 WAVEFORMS AND FREQUENCY CONTENT

The next step of evaluating the signals was to investigate the waveforms produced by the individual events. The waveforms for all acquired data are captured by the AEWin software, which can be viewed or extracted for further evaluation. For all three events, noted in the last section, waveforms from the six wideband sensors are shown in the following figures. A frequency spectrum for each waveform is also displayed next to them, which was calculated utilizing the Fast Fourier Transform (FFT), converting waveforms from the time domain to the frequency domain. The following figures (4.28-4.30) are in order of event, and hits are ordered numerically by sensor:

Many of the hit waveforms displayed possess similar characteristics to cracking in materials (including steel) found in existing literature (Amer et al. 2013). The waveforms closest to the source location are consistent with those of crack initiation to propagation (Amer et al. 2013). The cracking waveforms typically contain a sudden jump in energy immediately after initiation of the event, followed by attenuation of the signal thereafter. As a crack occurs in this case, a significant amount of potential energy stored in a stressed

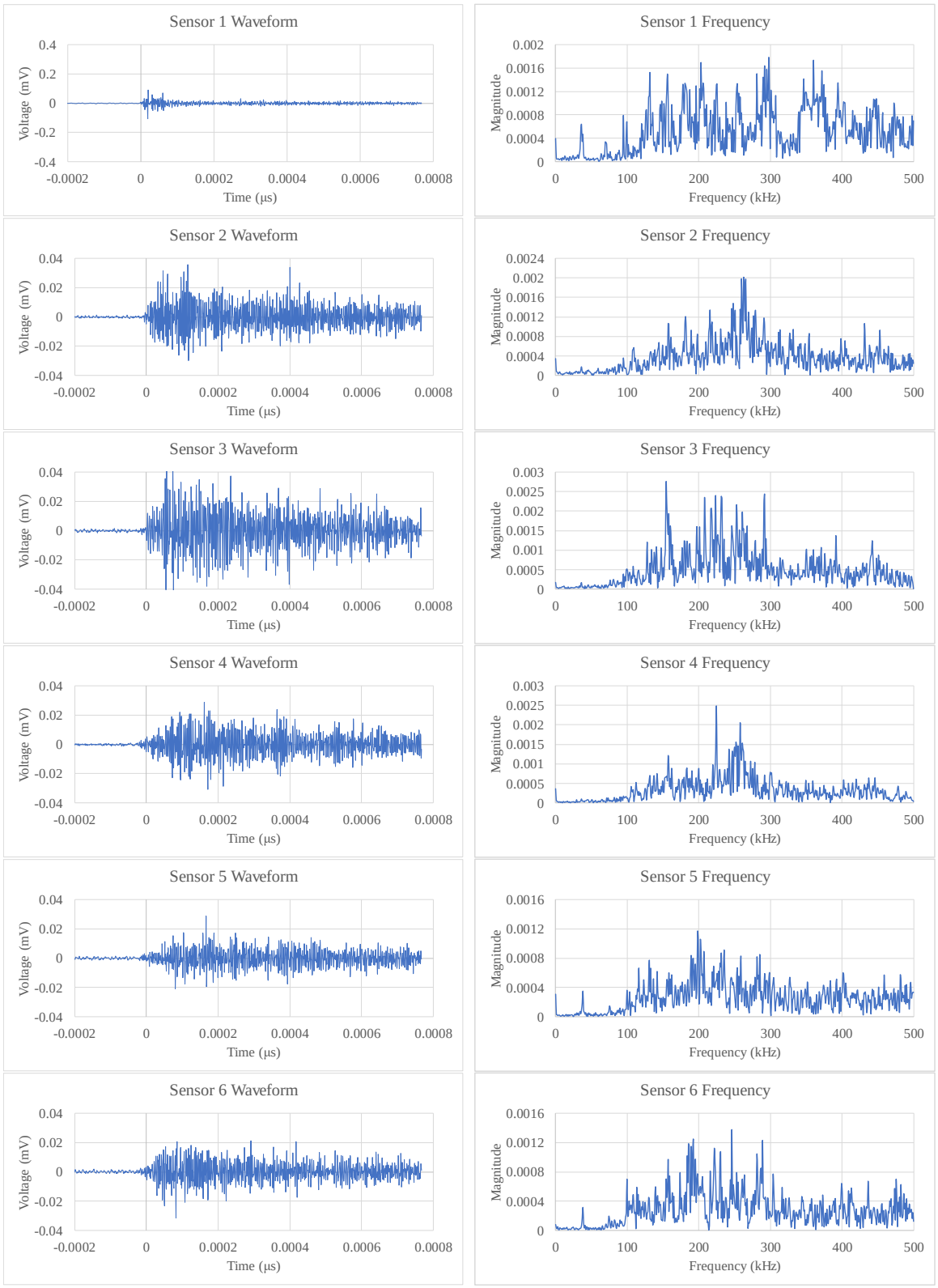


*Figure 4.28: Wideband waveforms and frequency spectrum for Event 1*

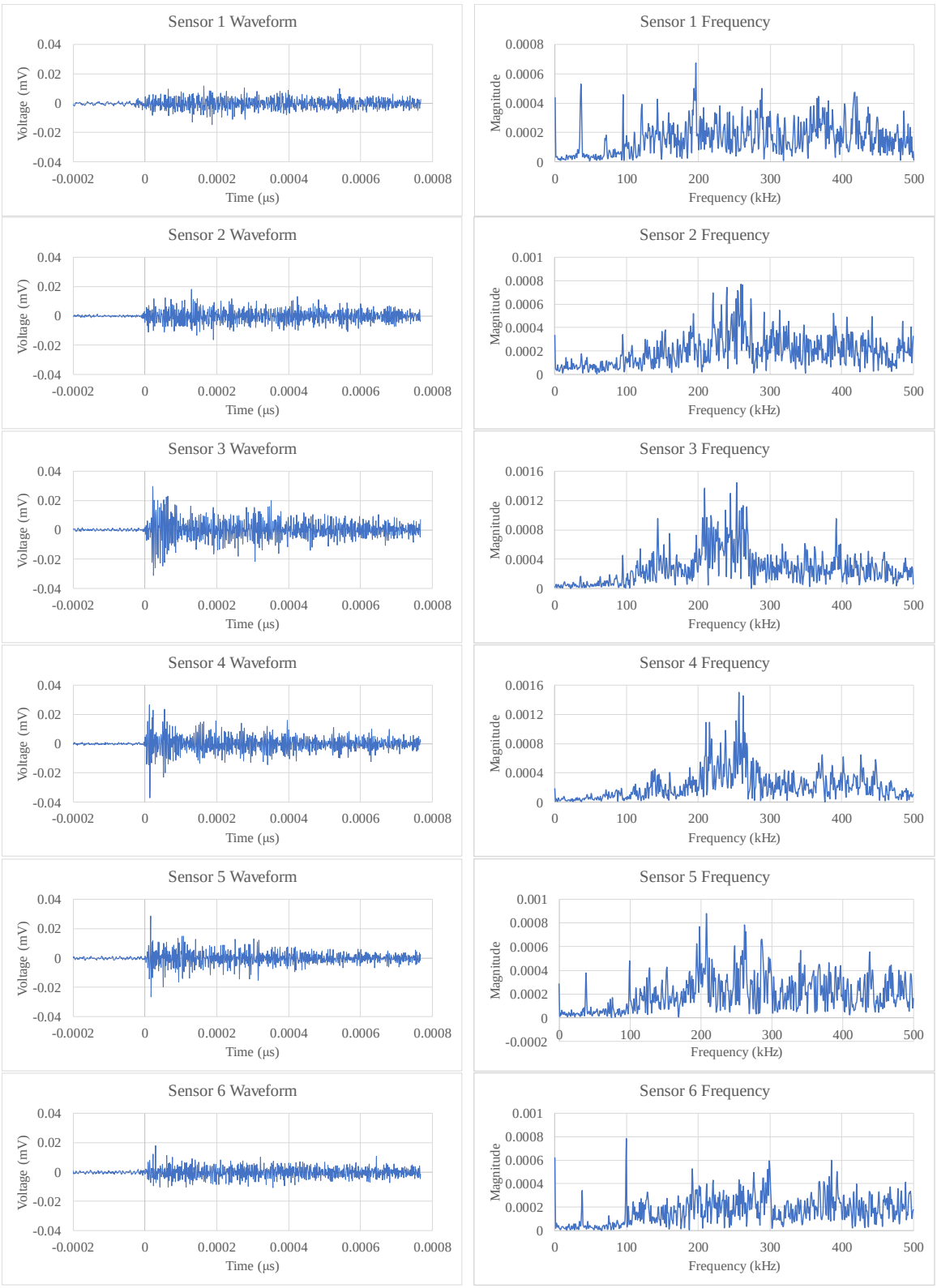


*Figure 4.29: Wideband waveforms and frequency spectrum for Event 2*

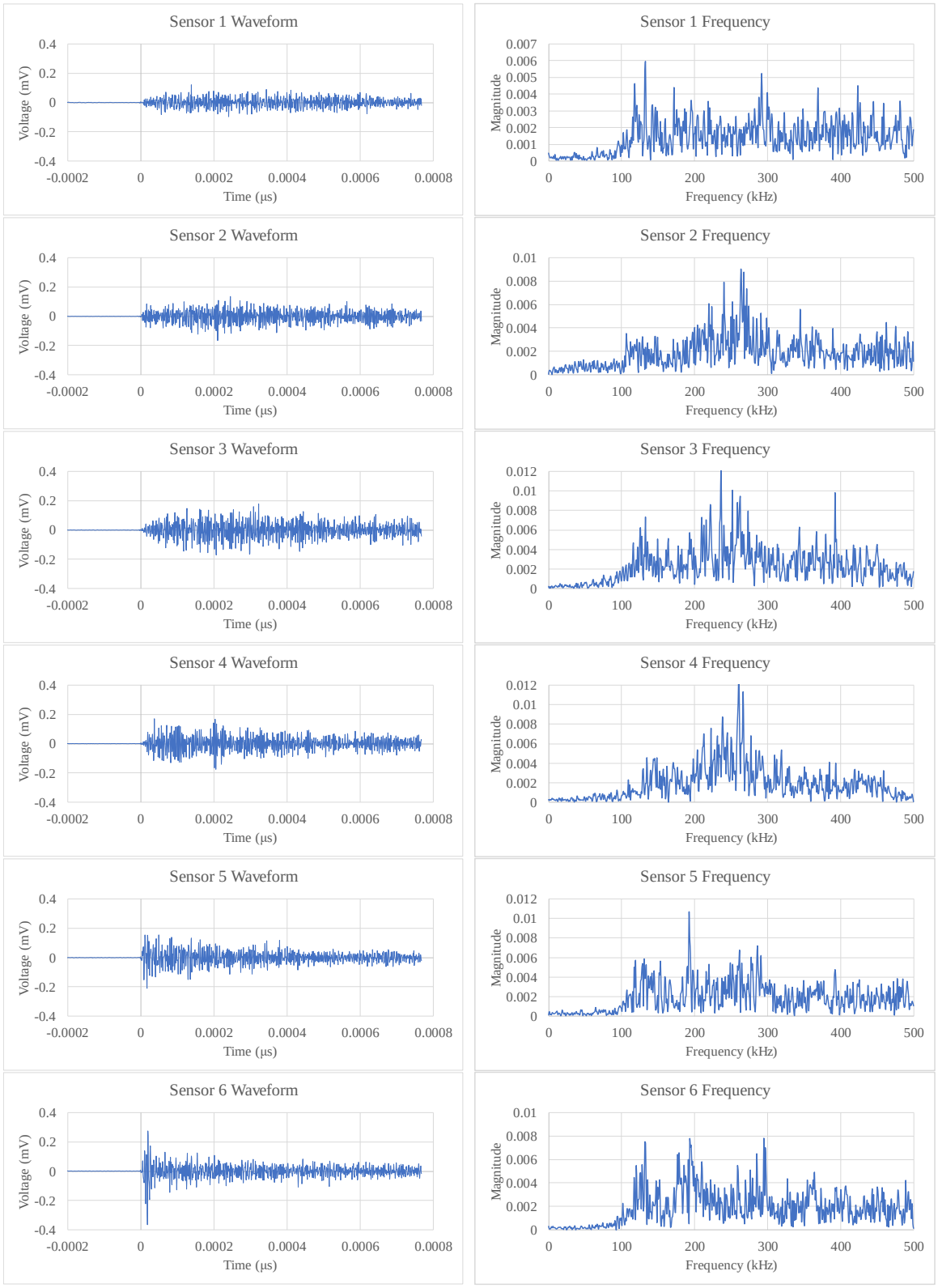


*Figure 4.30: Wideband waveforms and frequency spectrum for Event 3*

material is suddenly released, corresponding to a high initial jump in the sensor response during crack initiation. The energy is quickly dissipated through the material and the stress wave propagates away from the source location. As the wave reaches the other sensors placed on the sample, the energy magnitude is less than that of the sensor located closer to the source. This trend should continue as the wave reaches all remaining sensors attached to the sample. Hits occurring during the same period (around 100-200 microseconds) with much smaller amplitude energy are likely due to reflections of these waves as they encounter the boundaries of the physical material. Amer et al (2013) observed intergranular cracking in metal with higher quantities of hits and peak amplitudes in the range of 66-88 dB. Events 1-3 outlined in the above discussion have peak amplitudes near this range; all fall within 55-74 dB. It is noted that amplitudes are affected by source to sensor distance as well as material type and granularity.

The events in Figures 4.28-4.30 contain some waveforms that follow the characteristics described above, and some that diverge from this trend. Upon further examination of the time of arrival data (located in Figures 4.25-4.27), the events more representative of cracking are from sensors positioned closest to the source. The other waveforms produced during the same event by sensors situated further from the source, deviate from the expected cracking waveform pattern by not having the same large initial amplitude. This is likely due to attenuation or potentially associated with the large frequency range of the broadband sensors. Since the small-scale specimens only measure approximately one foot-square (relatively small for AE monitoring), interference from the outer boundaries (reflections) are another consideration.

FFT takes a time-based waveform signals and divides it into components along a

frequency domain, which may be useful for assessing the dominant frequency range for AE hits. This procedure was performed on the three sets of event waveforms above. The dominant frequency range (those of greatest magnitude) appears to be 100-300 kHz for the type 304 stainless-steel tested. The mean peak frequency for the tested material was determined to be approximately 244 kHz. More information related to this analysis is contained within Table 4.1. This frequency range, combined with numerical or analytical simulations, can be utilized for choosing more appropriate sensors for a large-scale test more representative in size of an actual DCSS canister.

*Table 4.1: Frequency characterization*

| **Peak Magnitude Frequency (kHz)** | | |
|---|---|---|
| Event 1 | Event 2 | Event 3 |
| 300 | 195 | 135 |
| 260 | 260 | 260 |
| 155 | 255 | 240 |
| 225 | 255 | 255 |
| 200 | 210 | 195 |
| 245 | 100 | 295 |
| **Frequency Range (kHz)** | | **100 to 300** |
| **Mean Peak Frequency (kHz)** | | **224** |
| **Standard Deviation (kHz)** | | **52.1** |

## 4.4 MICROSCOPY

Of the three events outlined above, the one which most definitively corresponds to cracking in the material is Event 2. This is due to its location near the EDM starter notch on the specimen (pictured in Figures 4.1 and 4.2). This location (right side of the notch in the diagrams), was visually monitored throughout the duration of testing with a Dino-Lite 10x-220x digital USB2.0 microscope. Figure 4.31 shows the notch of the specimen before any visually detectable cracking had occurred. Some microcracking may be present as the crack begins its propagation from a dark spot at the bottom of the notch noted in the figure

(noted with the arrow).

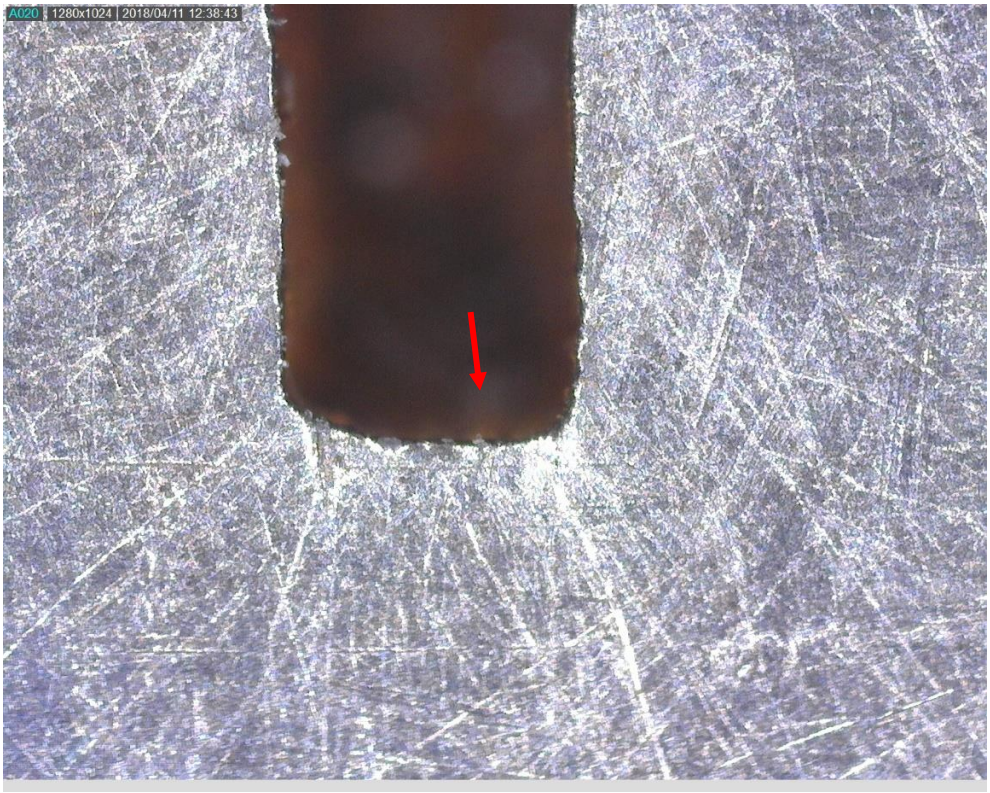


*Figure 4.31: Microscopic picture of notch before cracking, day 4 of 19*

As the specimen is exposed to the solution over time, visual evidence of crack growth begins to appear. Some cracking separation had begun Figure 4.32, which was taken five days after the initial picture. Figure 4.33 shows the same crack nineteen days after commencement of the test. At this point, the crack had visually lengthened toward the bottom of the picture. Figures 4.34 and 4.35 show the cracking path as it propagates further away from the visible notch and toward the edges of the plate.

The visible cracking along the central, tensile axis of the plate measures approximately 50.8 mm (2 in) in length, which includes cracks on either side of the notch and includes the length of the notch (0.5 in). The crack pictured in Figures 4.36 and 4.37 (L = crack width measurement) was measured using the proprietary Dino-Lite software to


*Figure 4.32: Initiation of cracking at notch at day 9 of 19*

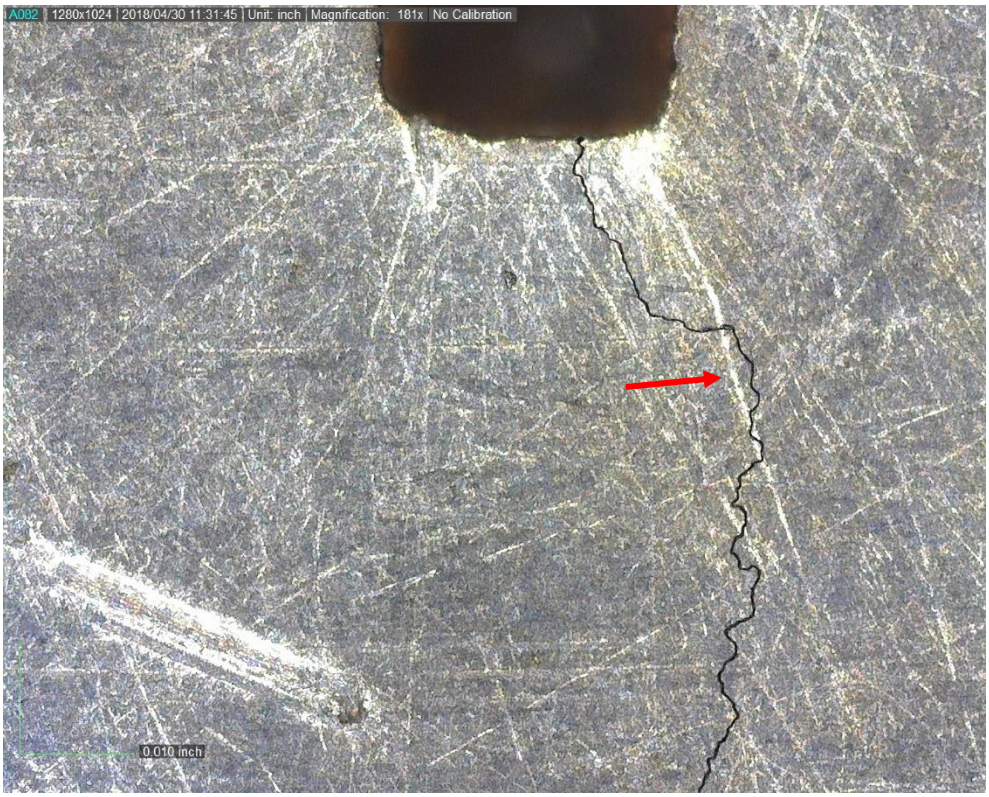


*Figure 4.33: Post cracking at notch at day 19*

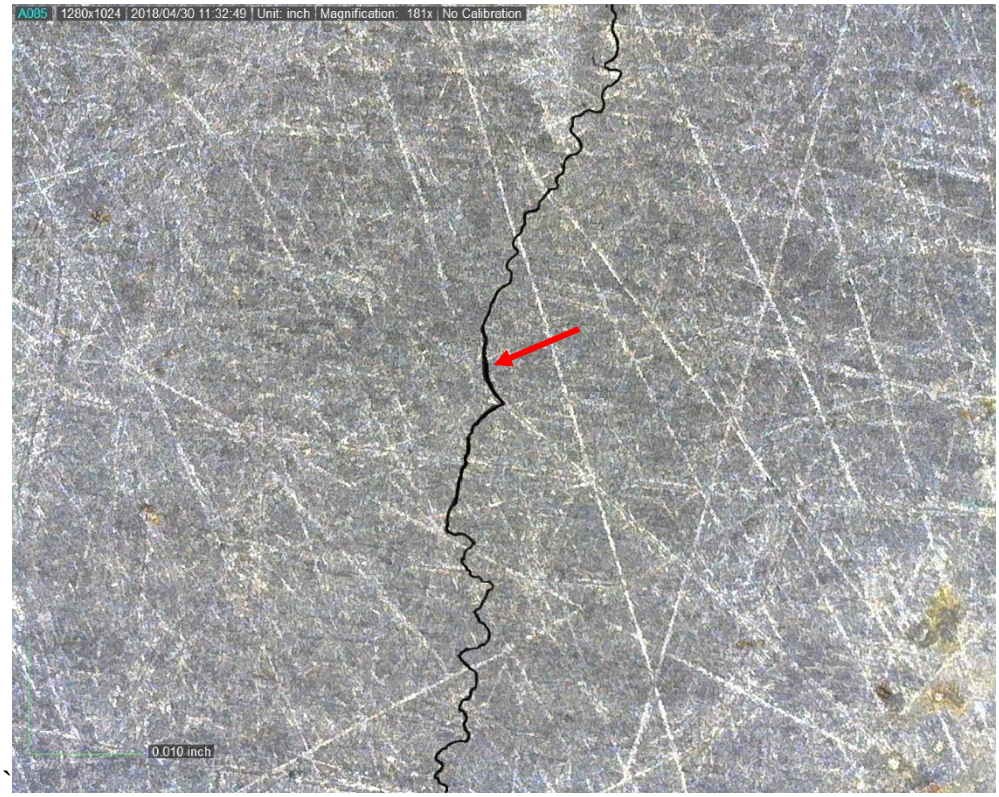


*Figure 4.34: Propagation of crack at notch continued at day 19*

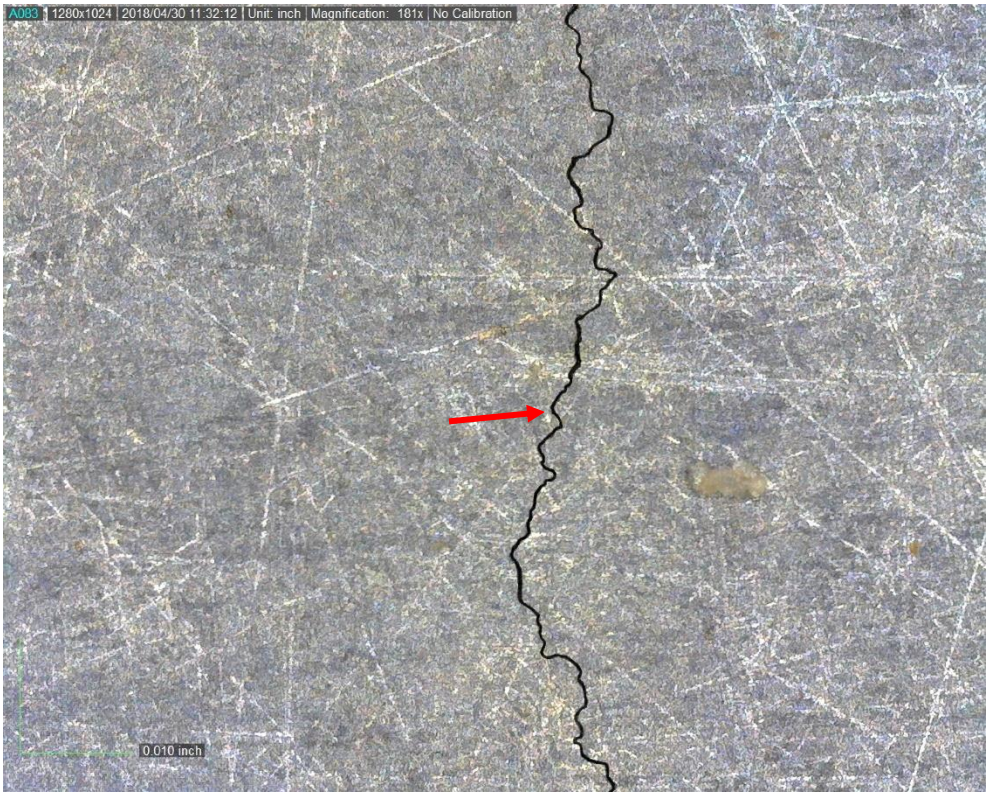


*Figure 4.35: Propagation of crack at notch continued at day 19*

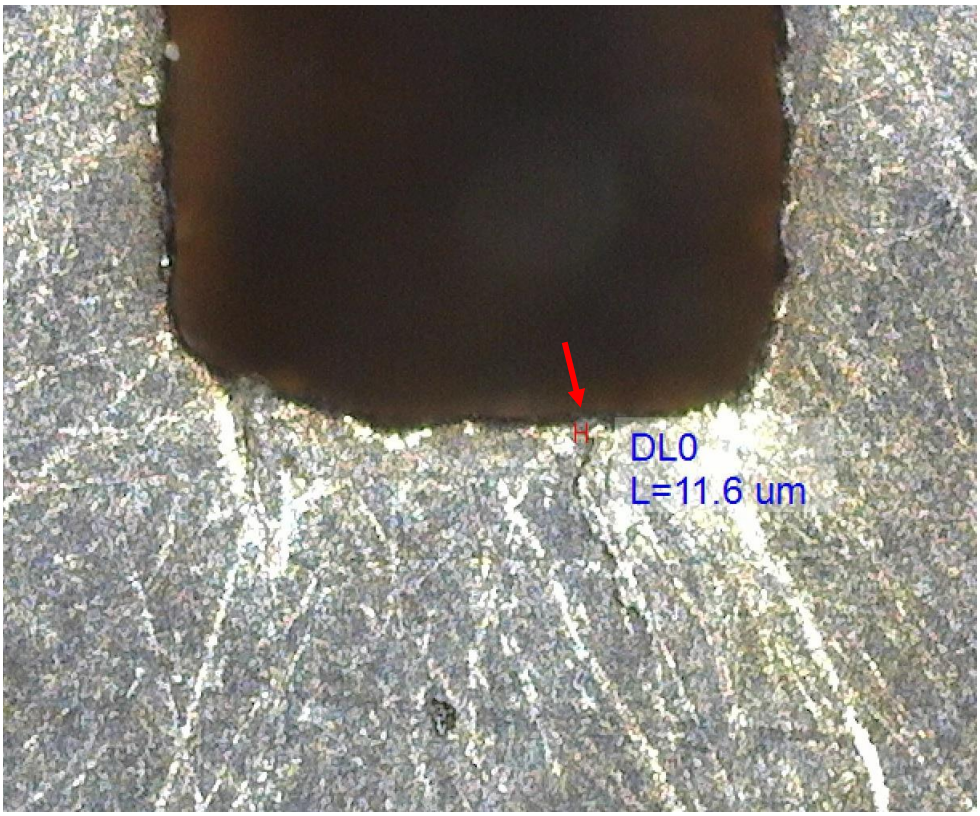


*Figure 4.36: Crack width at the starter notch at day 19*

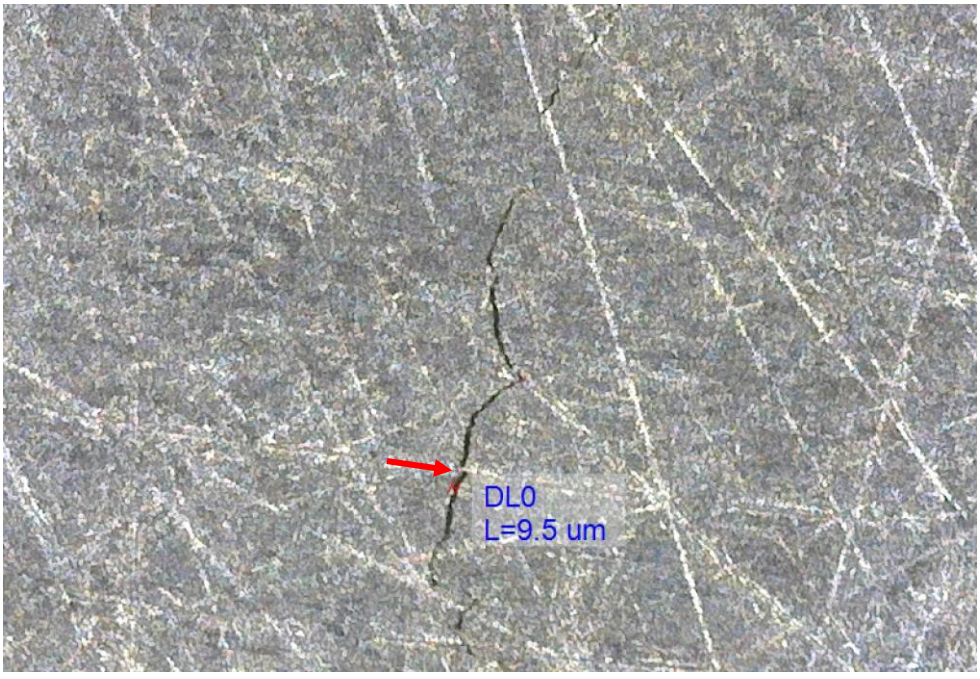


*Figure 4.37: Crack width at widest point at day 19*

be approximately 11.6 μm where it starts at the edge of the notch and measures approximately 9.5 μm at the widest point along the crack.

With the exception of Figure 4.31, all pictures shown were captured between day four and day nineteen of the active AE monitoring. The visual evidence of cracking, therefore, generally agrees with the crack events obtained through the acoustic emission monitoring procedure. Specifically, AE Event 2 and Event 3 are within this time period (Event 1 occurred prior to the photographs).

# CHAPTER 5. CONCLUSION

Storage of nuclear fuel has become challenging in past decades as permanent repositories have been delayed for various reasons. As spent fuel pools reach their capacity, fuel assemblies are often stored in temporary containers called Dry Cask Storage Systems (DCSS). These are large stainless-steel canisters surrounded by a protective layer of reinforced concrete and were originally intended for 20 years of use. Since the repositories have repeatedly been delayed, the canisters are being relicensed after inspection, and their use extended for further 40-year periods in some cases. Therefore, better monitoring and inspection techniques are desired, especially for casks housed in climates susceptible to high humidity and salinity levels. These environmental conditions exist in many nuclear facilities within coastal regions of the United States.

A possible solution for monitoring DCSS is the use of acoustic emission (AE) sensors since they can detect active material faults, such as cracking in metals. A single AE sensor per canister could potentially detect a crack in the canister wall or weld as it occurs and alert facility workers for further analysis or repairs. Furthermore, the use of three or more sensors provides for crack localization using triangulation of the wave from the event source.

This thesis discusses a small-scale crack growth detection test using a material (type 304H stainless-steel) and thickness similar to actual cask construction. Plate specimens underwent sensitization heat treatment for corrosion sensitivity and were statically loaded

to create tensile stresses at one face. A starter notch at the tensile surface was exposed to a corrosive solution of potassium tetrathionate ($K_2S_4O_6$) to induce cracking. The specimens were monitored for acoustic emission activity via six wideband differential AE sensors, two resonant AE sensors, DiSP workstation, and AEWin software interface for data acquisition and waveform feature extraction. The raw wideband data was filtered through visual inspection of waveforms and the resonant data filtered by hit count, duration, and signal strength. Distinct hits were singled out and their source located on the plate. Photographic evidence of cracking was captured before and after initiation from the starter notch. Progression of a crack at one end of the notch was monitored throughout the testing period.

Waveforms observed from the AE events due to the cracking displayed typical waveform patterns for initiation and propagation. Source location of AE activity was observed at cracks propagating from the starter notch, which displayed genuine waveform features. A frequency range of cracking events was determined using Fast Fourier Transform, and showed that the maximum magnitudes of genuine hits fell within a range of 100-300 kHz. The mean frequency of this sample was 224 kHz with a standard deviation of 52.1 kHz. Frequency range is useful for determining the best AE sensors for future field applications.

These results are from small-scale specimens (12” x 12.25” or 300 mm x 311 mm) and it is not fully demonstrated that they will correlate with waveforms and frequencies in a large-scale specimen more representative of an actual cask. Therefore, future work should be performed to investigate a similar procedure on a plate of similar thickness, with dimensions more representative of the typical height of the canisters. This future work will

provide further data to support the crack characteristics for type 304H and 304L stainless-steel materials used for DCSS. Other work to be completed includes full-scale specimens for similar crack growth and weld crack detection, pitting detection, further field testing at nuclear storage sites, and numerical modeling of stress wave propagation for specimens of similar geometry. This information will be useful for implementation of cask monitoring in the nuclear industry.

# REFERENCE


AEWin, Physical Acoustics. (2018). MISTRAS Group, Princeton, NJ

Aggelis, D. G., Kordatos, E. Z., and Matikas, T. E. (2011). "Acoustic emission for fatigue damage characterization in metal plates." Mechanics Research Communications, 38(2), 106–110.

Alvarez, M. G., Lapitz, P., and Ruzzante, J. (2008). "AE response of type 304 stainless steel during stress corrosion crack propagation." Corrosion Science, 50(12), 3382–3388.

Amer, A. O., Gloanec, A.-L., Courtin, S., and Touze, C. (2013). "Characterization of Fatigue Damage in 304L Steel by an Acoustic Emission Method." Procedia Engineering, 66, 651–660.

ASTM E1316-17a, Standard Terminology for Nondestructive Examinations, ASTM International, West Conshohocken, PA, 2017, www.astm.org

ASTM E976, Standard Guide for Determining the Reproducibility of Acoustic Emission Sensor Response, ASTM International, West Conshohocken, PA, 2017, www.astm.org

Ativitavas, N. (2002). "Acoustic emission signature analysis of failure mechanisms in fiber reinforced plastic structures." University of Texas Austin.

Babu, M. N., Mukhopadhyay, C. K., Sasikala, G., Albert, S. K., Bhaduri, A. K., Jayakumar, T., and Kumar, R. (2016). "Study of fatigue crack growth in RAFM steel using acoustic emission technique." Journal of Constructional Steel Research, 126, 107–116.

BSSA: British Stainless Steel Associatin (n.d.). "Corrosion mechanisms in stainless steel." (n.d.). <https://www.bssa.org.uk/topics.php?article=95> (Jan. 10, 2018).

Chen, C., Zhang, B., and Vachtsevanos, G. (2012). "Prediction of Machine Health Condition Using Neuro-Fuzzy and Bayesian Algorithms." IEEE Transactions on Instrumentation and Measurement, 61(2), 297–306.

Danyuk, A., Rastegaev, I., Pomponi, E., Linderov, M., Merson, D., and Vinogradov, A. (2017). "Improving of Acoustic Emission Signal Detection for Fatigue Fracture Monitoring." Procedia Engineering, 176, 284–290.

Du, G., Li, J., Wang, W. K., Jiang, C., and Song, S. Z. (2011). "Detection and characterization of stress-corrosion cracking on 304 stainless steel by electrochemical noise and acoustic emission techniques." Corrosion Science, 53(9), 2918–2926.

Hossain, M., J. Yu, P. Ziehl, J. Caicedo (2012). "Acoustic emission source characterization of fatigue crack extension in steel bridge material." American Institute of Physics, Vol. 1511, 1378-1384.

Ghosh, S., and Kain, V. (2010). "Microstructural changes in AISI 304L stainless steel due to surface machining: Effect on its susceptibility to chloride stress corrosion cracking." Journal of Nuclear Materials, 403(1-3), 62–67.

Gomez-Duran, M., and Macdonald, D. D. (2006). "Stress corrosion cracking of sensitized Type 304 stainless steel in thiosulphate solution. II. Dynamics of fracture." Corrosion Science, 48(7), 1608–1622.

Greer, B., Ziehl, P., (2016) "Nondestructive evaluation: Investigation of acoustic emission technologies for monitoring inaccessible regions of dry fuel storage systems." Electric Power Research Institute, Technical Report

Li, R., and He, D. (2012). "Rotational Machine Health Monitoring and Fault Detection Using EMD-Based Acoustic Emission Feature Quantification." IEEE Transactions on Instrumentation and Measurement, 61(4), 990–1001.

Lapitz, P., Ruzzante, J., Alvarez, M.G. (2007) "AE response of a-brass during stress corrosion crack propagation." Corrosion Science. 49 (2007) 3812–3825.

Loutas, T.H. , Sotiriades, G. , Kalaitzoglou, I. , Kostopoulos, V. (2009). "Condition monitoring of a single-stage gearbox with artificially induced gear cracks utilizing on-line vibration and acoustic emission measurements", Applied Acoustics, 70 (2009) 1148–1159

Marrow, T. J., Babout, L., Jivkov, A. P., Wood, P., Engelberg, D., Stevens, N., Withers, P. J., and Newman, R. C. (2006). "Three dimensional observations and modelling of intergranular stress corrosion cracking in austenitic stainless steel." Journal of Nuclear Materials, 352(1-3), 62–74.

Mazal, P., Vlasic, F., and Koula, V. (2015). "Use of Acoustic Emission Method for Identification of Fatigue Micro-Cracks Creation." Procedia Engineering, 133, 379–388.

McKeefry, J., Shield, C. (1999). “Acoustic Emission Monitoring of Fatigue Cracks in Steel Bridge Girders.” Minnesota Department of Transportation and University of Minnesota

NOESIS, Physical Acoustics. (2018). MISTRAS Group, Princeton, NJ

Qu, Y., He, D., Yoon, J., Van Hecke, B., Bechhoefer, E., and Zhu, J. (2014). “Gearbox Tooth Cut Fault Diagnostics Using Acoustic Emission and Vibration Sensors — A Comparative Study.” Sensors, 14(1), 1372–1393.

Raj, B., Subramanian, C. V., Jayakumar, T (2000). *Non-destructive Testing of Welds*, Narosa, New Delhi

SLER: State and Local Energy Report (2013) “The Problem with Yucca Mountain” <http://stateenergyreport.com/2013/05/21/the-problem-with-yucca-mountain/> (Jan. 10, 2018).

Shaikh, H., Amirthalingam, R., Anita, T., Sivaibharasi, N., Jaykumar, T., Manohar, P., Khatak, H.S. (2007). “Evaluation of Stress corrosion cracking phenomenon in an AISI type 316LN stainless steel using acoustic emission technique” Corrosion Science 49 (2007) 740-765

Turnbull, A., Mingard, K., Lord, J. D., Roebuck, B., Tice, D. R., Mottershead, K. J., Fairweather, N. D., and Bradbury, A. K. (2011). “Sensitivity of stress corrosion cracking of stainless steel to surface machining and grinding procedure.” Corrosion Science, 53(10), 3398–3415.

USEIA: United States Energy Information Administration (2017) “What is U.S. electricity generation by energy source?” <https://www.eia.gov/tools/faqs/faq.php?id=427&t=3> (Mar. 4, 2018)

UCS: Union of Concerned Scientists (2013) “The Growing Threat of Nuclear Waste | Union of Concerned Scientists.” (n.d.). <https://www.ucsusa.org/publications/catalyst/su-13-the-growing-threat-of-nuclear-waste.html> (Mar. 4, 2018).

USNRC: U.S. Nuclear Regulatory Commission (2017). “NRC: Dry Cask Storage.” <https://www.nrc.gov/waste/spent-fuel-storage/dry-cask-storage.html> (Jan. 10, 2018).

Yu, J., and Ziehl, P. (2012). “Stable and unstable fatigue prediction for A572 structural steel using acoustic emission.” Journal of Constructional Steel Research, 77, 173–179.

Yu, J., Ziehl, P., Matta, F., and Pollock, A. (2013). “Acoustic emission detection of fatigue damage in cruciform welded joints.” Journal of Constructional Steel Research, 86, 85–91.

Yu, J., Ziehl, P., Zárate, B., and Caicedo, J. (2011). “Prediction of fatigue crack growth in steel bridge components using acoustic emission.” Journal of Constructional Steel Research, 67(8), 1254–1260.

# APPENDIX A. PLATE LOADING AND STRESS CALCULATION

Stresses were calculated at the axis along the EDM notch located at the top face of plate specimen. The geometric and material properties were:

$h = 0.625\ in$ $\quad b = 12\ in$ $\quad A = h \cdot b = 7.500\ in^2$

$c = \frac{h}{2} = 0.313\ in$ $\quad I = \frac{b \cdot h^3}{12} = 0.221\ in^4$ $\quad arm = 3\ in + c = 3.313\ in$

$\sigma_y = 30{,}000\ psi$ $\quad \sigma_{target} = 27{,}000\ psi$ $\quad E = 28{,}500{,}000\ psi$

Where the height ($h$) and width ($b$) were used to determine the cross-sectional area ($A$), the distance to the neutral axis ($c$) form either extreme fiber, and the moment of inertia ($I$). The moment arm (arm) is the distance from the bolt to the desired point of stress determination. Other properties used for the type 304 stainless-steel specimen are the yielding stress ($\sigma_y$), the modulus of elasticity ($E$), and a target stress ($\sigma_{target}$) for this procedure that is less than yielding.

Using the maximum normal stress equation,

$$\sigma = \frac{P}{A} + \frac{M \cdot c}{I}$$

$$\sigma = \frac{P}{A} + \frac{P \cdot arm \cdot c}{I}$$

the load for target stress in the extreme tensile fiber can be determined by rearranging.

$$P_{tension} = \frac{\sigma_{target}}{\left(-\frac{1}{A} + \frac{arm \cdot c}{I}\right)} = 6{,}575\ lb$$

Likewise, load for target stress in the extreme compressive fiber is:

$$P_{compression} = \frac{-\sigma_{target}}{\left(-\frac{1}{A} - \frac{arm \cdot c}{I}\right)} = 6{,}174\ lb$$

Therefore, the compressive stress governs the specimen loading since it will be reached first. Then the corresponding stresses were determined.

$$M = P_{compression} \cdot arm = 20{,}451\ lb \cdot in$$

$$\sigma_{top} = -\frac{P_{compression}}{A} + \frac{M \cdot c}{I} = 25{,}354\ psi$$

$$\sigma_{bottom} = -\frac{P_{compression}}{A} - \frac{M \cdot c}{I} = 27{,}000\ psi$$

The resulting strain in the top fiber, thus at the axis along the notch is:

$$\varepsilon_{top} = \frac{\sigma_{top}}{E} = 870\ x\ 10^{6}$$

This is the target strain reading from the strain gauges that determined proper loading on the plate specimens. The strain reading was monitored while loading the bottom bolt with a manual torque wrench. The torque required can be determined using the bolt diameter (*D*), a nut factor for lubricated situations (*k*), and the compressive force determined above (*F*).

$D = 0.75\ in$ $\quad$ $k = 0.180\ in$ $\quad$ $F = P_{compression} = 6{,}474\ lb$

The torque placed on the bolt was determined using the following equation:

$$T = k \cdot D \cdot F = 883\ lb \cdot in$$

$$T = k \cdot D \cdot \left(\frac{ft}{12\ in}\right) \cdot F = 69.5\ lb \cdot ft$$

# APPENDIX B. PLATE LOADING AND BOLT TORQUE TABLE

| Load | | Bolt Torque | | Bolt Torque | |
|---|---|---|---|---|---|
| 500.00 | lb | 67.50 | lb-in | 5.63 | lb-ft |
| 1,000.00 | lb | 135.00 | lb-in | 11.25 | lb-ft |
| 1,500.00 | lb | 202.50 | lb-in | 16.88 | lb-ft |
| 2,000.00 | lb | 270.00 | lb-in | 22.50 | lb-ft |
| 2,500.00 | lb | 337.50 | lb-in | 28.13 | lb-ft |
| 3,000.00 | lb | 405.00 | lb-in | 33.75 | lb-ft |
| 3,500.00 | lb | 472.50 | lb-in | 39.38 | lb-ft |
| 4,000.00 | lb | 540.00 | lb-in | 45.00 | lb-ft |
| 4,500.00 | lb | 607.50 | lb-in | 50.63 | lb-ft |
| 5,000.00 | lb | 675.00 | lb-in | 56.25 | lb-ft |
| 5,500.00 | lb | 742.50 | lb-in | 61.88 | lb-ft |
| 6,000.00 | lb | 810.00 | lb-in | 67.50 | lb-ft |
| 6,174.00 | lb | 833.49 | lb-in | 69.46 | lb-ft |
| 6,500.00 | lb | 877.50 | lb-in | 73.13 | lb-ft |
| 7,000.00 | lb | 945.00 | lb-in | 78.75 | lb-ft |
| 7,500.00 | lb | 1,012.50 | lb-in | 84.38 | lb-ft |
| 8,000.00 | lb | 1,080.00 | lb-in | 90.00 | lb-ft |
| 8,500.00 | lb | 1,147.50 | lb-in | 95.63 | lb-ft |
| 9,000.00 | lb | 1,215.00 | lb-in | 101.25 | lb-ft |
| 9,500.00 | lb | 1,282.50 | lb-in | 106.88 | lb-ft |
| 10,000.00 | lb | 1,350.00 | lb-in | 112.50 | lb-ft |
| 10,500.00 | lb | 1,417.50 | lb-in | 118.13 | lb-ft |
| 11,000.00 | lb | 1,485.00 | lb-in | 123.75 | lb-ft |
| 11,500.00 | lb | 1,552.50 | lb-in | 129.38 | lb-ft |
| 12,000.00 | lb | 1,620.00 | lb-in | 135.00 | lb-ft |
| 12,500.00 | lb | 1,687.50 | lb-in | 140.63 | lb-ft |
| 13,000.00 | lb | 1,755.00 | lb-in | 146.25 | lb-ft |

$D = 0.75\ in$ $k = 0.180\ in$ $F = P_{compression} = 6{,}474\ lb$

$$T = k \cdot D \cdot F = 883\ lb \cdot in$$

$$T = k \cdot D \cdot \left(\frac{ft}{12\ in}\right) \cdot F = 69.5\ lb \cdot ft$$